

# Underestimated MJO variability in CMIP6 models

Phong Vu Viet Le<sup>1</sup>, Clement Guilloteau<sup>2</sup>, Antonios Mamalakis<sup>3</sup>, and Efi Foufoula-Georgiou<sup>1</sup>

<sup>1</sup>University of California, Irvine

<sup>2</sup>UC Irvine

<sup>3</sup>University of California Irvine

November 28, 2022

## Abstract

The Madden-Julian Oscillation (MJO) is the leading mode of intra-seasonal climate variability, having profound impacts on a range of weather and climate phenomena. Here, we use a wavelet-based spectral Principal Component Analysis (wsPCA) to evaluate the skill of 20 state-of-the-art CMIP6 models in capturing the magnitude and dynamics of the MJO. The advantages of wsPCA are its ability to focus on desired frequencies and capture each propagative physical mode with one principal component (PC). We show that the MJO contribution to the total intra-seasonal climate variability is substantially underestimated in most CMIP6 models. The joint distribution of the modulus and angular frequency of the complex wavelet PC series associated with MJO is used to rank models relatively to the observations through the Wasserstein distance. Using Hovmöller phase-longitude diagrams, we show that precipitation variability associated with MJO is underestimated in most CMIP6 models for the Amazonia, Southwest Africa, and Maritime Continent.

1

2

## Underestimated MJO variability in CMIP6 models

3

4 **Phong V.V. Le<sup>1,2</sup>, Clement Guilloteau<sup>1</sup>, Antonios Mamalakis<sup>1,3</sup>, and Efi Foufoula-**  
5 **Georgiou<sup>1,4</sup>**

6

7 <sup>1</sup>Department of Civil and Environmental Engineering, University of California Irvine, CA, USA

8 <sup>2</sup>Faculty of Hydrology Meteorology and Oceanography, University of Science, Vietnam National  
9 University, Hanoi, Vietnam

10 <sup>3</sup>Department of Atmospheric Science, Colorado State University, Fort Collins, CO, USA

11 <sup>4</sup>Department of Earth Systems Science, University of California Irvine, CA, USA

12

13 Corresponding author: Phong V.V. Le ([phongl3@uci.edu](mailto:phongl3@uci.edu)); Efi Foufoula-Georgiou ([efi@uci.edu](mailto:efi@uci.edu))

14

### 15 **Key Points:**

- 16 • A wavelet-based spectral principal component analysis is used to examine CMIP6  
17 models in reproducing the Madden-Julian Oscillation (MJO)
- 18 • CMIP6 models capture the average MJO propagation speed but significantly  
19 underestimate the MJO contribution to the total intra-seasonal climate variability
- 20 • Precipitation variability related to MJO over the Amazonia, Southwest Africa, and  
21 Maritime Continent is underestimated in CMIP6 models

22

23 *The manuscript is under review in Geophysical Research Letters.*

24 **Date:** January 9, 2021

**25 Abstract**

26 The Madden-Julian Oscillation (MJO) is the leading mode of intra-seasonal climate variability,  
27 having profound impacts on a wide range of weather and climate phenomena. Here, we use a  
28 wavelet-based spectral Principal Component Analysis (wsPCA) to evaluate the skill of 20 state-  
29 of-the-art CMIP6 models in capturing the magnitude and dynamics of the MJO. The advantages  
30 of wsPCA are its ability to focus on desired frequencies and capture each propagative physical  
31 mode with one principal component (PC). We show that the MJO contribution to the total intra-  
32 seasonal climate variability is substantially underestimated in most CMIP6 models. The joint  
33 distribution of the modulus and angular frequency of the complex wavelet PC series associated  
34 with MJO is used to rank models relatively to the observations through the Wasserstein distance.  
35 Using Hovmöller phase-longitude diagrams, we also show that precipitation variability associated  
36 with MJO is underestimated in most CMIP6 models for the Amazonia, Southwest Africa, and  
37 Maritime Continent.

38

39

**40 Plain Language Summary**

41 Dominant modes (i.e. coherent spatio-temporal patterns of variability) of the climate system, such  
42 as the Madden-Julian Oscillation (MJO), influence a wide range of weather and climate  
43 phenomena worldwide. The ability of state-of-the-art climate models to accurately simulate these  
44 modes is crucial for advancing our understanding of the climate system and reliably predicting its  
45 future trends. The Coupled Model Intercomparison Project phase 6 (CMIP6) will be the foundation  
46 for the upcoming Intergovernmental Panel on Climate Change (IPCC) Sixth Assessment Report.  
47 Here, we use a wavelet-based spectral principal component analysis (wsPCA) to quantitatively  
48 assess how well historical simulations from 20 CMIP6 models capture MJO as compared to  
49 observations. We first show that the MJO magnitude is not reproduced well in most of CMIP6  
50 models. We then reveal that MJO-related precipitation variability in the Amazonia, Southwest  
51 Africa, and Maritime Continent is significantly underestimated in many CMIP6 models. Our  
52 results highlight the need to better simulate the coupled ocean-atmosphere dynamics in order to  
53 improve the representation of MJO in climate models. Moreover, studies using projected states of  
54 MJO for assessing future tropical and extratropical impacts should be examined with caution.

## 55 1. Introduction

56 The Madden-Julian Oscillation (MJO) is the dominant mode of intra-seasonal (1-3 months)  
57 variability in the tropical atmosphere, characterized by an eastward-moving band of rain clouds  
58 (Madden & Julian, 1971, 1972). The MJO interacts with a wide range of tropical weather and  
59 climate phenomena, including monsoonal systems (Lorenz & Hartmann, 2006; Taraphdar et al.,  
60 2018), tropical cyclone activity (Bessafi & Wheeler, 2006; Klotzbach, 2010; Maloney &  
61 Hartmann, 2000), and the El Niño-Southern Oscillation (ENSO) (Hendon et al., 2007; Lau &  
62 Waliser, 2012; Takayabu et al., 1999). As a strong tropical heating source, the MJO also exhibits  
63 teleconnections to the extratropics affecting regional hydroclimate (Jones et al., 2004; Roxy et al.,  
64 2019). Given the planetary-scale climatic impacts of the MJO, the ability of state-of-the-art  
65 coupled general circulation models (CGCMs) to accurately capture its magnitude, location and  
66 dynamics is of vital importance for subseasonal-to-seasonal prediction (Robertson et al., 2015;  
67 Woolnough, 2019) and assessment of future global climate (Meehl, Stocker, et al., 2007).

68 A number of efforts have focused on assessing CGCMs, primarily those participating in  
69 the Coupled Model Intercomparison Projects (CMIP) (Lambert & Boer, 2001; Meehl, Covey, et  
70 al., 2007; Taylor et al., 2012) in terms of their ability to properly capture organized spatio-temporal  
71 modes across scales. Despite much progress in climate modeling, considerable shortcomings in  
72 simulating major modes of climate variability remain, persisting from one model generation to the  
73 next (Eyring et al., 2019). For instance, at intra-seasonal timescales, previous generation CGCMs  
74 typically exhibit poor representation of MJO dynamics both in amplitude and the eastward  
75 propagating pattern (Ahn et al., 2017; Hung et al., 2013; Jiang et al., 2015; Lin et al., 2006; Zhang  
76 et al., 2006). The primary factors hypothesized to affect MJO simulations in CGCMs include  
77 model resolution and physics, especially the air-sea coupling across multiple spatial scales (Jiang  
78 et al., 2020; Zhang, 2005).

79 The CMIP6 set of models (Eyring et al., 2016) will be the foundation for the  
80 Intergovernmental Panel on Climate Change Sixth Assessment Report. Featuring substantial  
81 improvements in the physical parameterizations and inclusion of additional Earth system  
82 processes, the CMIP6 is expected to provide a rich opportunity to evaluate the aforementioned  
83 shortcomings in simulating MJO. Thus far, very few studies have investigated the performance of  
84 CMIP6 models in capturing the MJO. Recently, Orbe et al. (2020) analyzed six U.S. climate  
85 models participating in CMIP6 and reported improvements in the amplitudes of the MJO-related  
86 winds and precipitation compared to the CMIP5. By analyzing 34 models, Ahn et al. (2020)  
87 showed that the propagation of MJO over the Maritime Continent in CMIP6 models is more  
88 realistic than in the CMIP5. The connection between MJO and the quasi-biennial oscillation  
89 (QBO) in CMIP6 models has also been explored (Kim et al., 2020). Nevertheless, there is still a  
90 general lack of understanding of the MJO representation in the state-of-the-art climate models.

91 Two classical ways of identifying MJO dynamics is through a space-time spectral analysis  
92 (STSA) (Hendon & Wheeler, 2008; Kiladis et al., 2005; Wheeler & Kiladis, 1999) and an  
93 empirical orthogonal function (EOF) analysis (Lo & Hendon, 2000; Maloney & Hartmann, 1998;  
94 Waliser et al., 2003; Wheeler & Hendon, 2004). While the STSA requires the selection of windows  
95 in the wavenumber-frequency domain containing the signal of interest, EOF-based methods  
96 require bandpass filtering and seasonal partitioning to isolate the intra-seasonal components of the  
97 data. The frequency-domain (spectral) variants of EOF analysis (Hannachi et al., 2007; Schmidt  
98 et al., 2019) rely on the eigen-decomposition of the Fourier cross-spectral matrix (CSM), which  
99 offers the possibility to look for modes in specific frequency bands and handle propagating effects.

100 We propose to use the wavelet-based spectral principal component analysis (wsPCA), which is  
 101 based on the eigen-decomposition of the CSM computed through a continuous complex analytic  
 102 wavelet transform (Guilloteau et al., 2020). The wsPCA allows robust estimation of the CSM and  
 103 seamlessly removes trends in the data without any pre-processing. The complex wavelet principal  
 104 component (wPC) time series resulting from the wsPCA are characterized by their instantaneous  
 105 magnitude and phase, which are useful quantities to describe the temporal evolution of dynamical  
 106 climatic modes.

107 In this study, we analyze global precipitation (PPT) and outgoing longwave radiation  
 108 (OLR) daily time series to assess MJO variability in observations, reanalysis, and as simulated by  
 109 20 CMIP6 models under historical forcing. Particularly, we first demonstrate the use of the wsPCA  
 110 to robustly extract the spatio-temporal patterns of the MJO. We then evaluate the dynamics of  
 111 MJO simulated in CMIP6 models by comparing them to those inferred by the observations.  
 112 Finally, we evaluate MJO-related precipitation variability as simulated by CMIP6 models in the  
 113 Amazonia, Southwest Africa, and Maritime Continent. The rest of this paper is organized as  
 114 follows. Section 2 describes the data and methodology used. Section 3 presents the main results of  
 115 this study followed by a summary in Section 4.

## 116 2. Materials and Methods

### 117 2.1. Data

118 **CMIP6 Models:** Daily-averaged outputs, including PPT and OLR, from historical  
 119 simulations of 20 CMIP6 models (Table S1) during the period 1983-2014 are examined. Model  
 120 output is taken only from the first ensemble member (r1i1p1f1) of each model, which uses the  
 121 same observed evolution of forcing in the 20<sup>th</sup> century. All model outputs are bilinearly  
 122 interpolated to a common equal-area scalable earth (EASE) grid of approximately 220 km  
 123 resolution (Brodzik et al., 2014). Anomaly time series of each field are obtained by removing the  
 124 climatic mean of each day of the year (DOY) from the raw data. The climatic mean is calculated  
 125 as the average over the study period of the 15-day period centered on each DOY.

126 **Observations and Reanalysis:** For observations, we employ the daily global interpolated  
 127 OLR obtained from the National Center for Atmospheric Research. Daily PPT is obtained from  
 128 the PERSIANN-CDR database (Ashouri et al., 2015). For reanalysis, daily-averaged fields of the  
 129 above variables are obtained from the ERA5 datasets (Hersbach et al., 2020). Observations and  
 130 reanalysis datasets are obtained over the same period (1983-2014) and interpolated onto the same  
 131 EASE grid as CMIP6 models for comparison. Moreover, daily observed precipitation obtained  
 132 from other datasets (TRMM, IMERG, GPCP, and CMORPH) is used for comparison with the  
 133 PERSIANN-CDR (Table S2).

### 134 2.2. Methodology

135 We use the wsPCA (Guilloteau et al., 2020) to identify organized spatio-temporal modes  
 136 of variability within the MJO timescales. The wsPCA relies on the estimation of the CSM between  
 137 time series at different locations using the Morlet continuous wavelet transform (CWT) and the  
 138 extraction of its eigenvectors in various frequency bands. Consider a dataset consisting of  $L$  time-  
 139 ordered snapshots of a variable at  $N$  gridded locations,  $\mathbf{X} = (\mathbf{x}_1, \mathbf{x}_2, \dots, \mathbf{x}_N)^T \in \mathbb{R}^{N \times L}$ . The  $i^{\text{th}}$  row  
 140 of  $\mathbf{X}$ , that is  $\mathbf{x}_i^T = (x_{i,t_1}, \dots, x_{i,t_L}) \in \mathbb{R}^L$ , represents the time series at the  $i^{\text{th}}$  location. Meanwhile,

141 the  $j^{\text{th}}$  column  $(x_{1,t_j}, \dots, x_{N,t_j})^T \in \mathbb{R}^N$  represents the vectorized snapshot at time  $t_j$ . The CWT of  
 142  $\mathbf{x}_i$  is defined as  $w_i(\nu, t) = \frac{1}{\sqrt{\nu}} \int_{-\infty}^{+\infty} x_i(\tau) \Psi^* \left( \frac{\tau-t}{\nu} \right) d\tau$ , where  $\Psi^*(t)$  is the complex conjugate of the  
 143 Morlet wavelet defined in its simplified form as  $\Psi(t) \approx \pi^{-\frac{1}{4}} e^{i2\pi f_0 t} e^{-\frac{t^2}{2}}$ ,  $\nu$  is the scale parameter,  
 144 and  $f_0$  is the central frequency of the Morlet wavelet (Addison, 2002). We choose  $f_0 = \sqrt{\frac{1}{2 \ln 2}}$ ,  
 145 often used in practice when accurate time localization of the wavelet transform is sought. At the  
 146 scale  $\nu$ , corresponding to the Fourier frequency  $f = \frac{f_0}{\nu}$ , the CWT of all  $\mathbf{x}_i$  time series can be  
 147 arranged into a matrix of wavelet coefficients:

$$\mathbf{W}_f = \begin{bmatrix} w_1(f, t_1) & \cdots & w_1(f, t_L) \\ \vdots & \ddots & \vdots \\ w_N(f, t_1) & \cdots & w_N(f, t_L) \end{bmatrix} \in \mathbb{C}^{N \times L} \quad (1)$$

148 The empirical CSM at frequency  $f$  is then computed as  $\mathbf{S}_f = \frac{1}{L-1} \mathbf{W}_f \mathbf{W}_f' \in \mathbb{C}^{N \times N}$  and its eigen-  
 149 decomposition constitutes the wsPCA:

$$\mathbf{S}_f \mathbf{U}_f = \mathbf{U}_f \mathbf{\Lambda}_f \quad (2)$$

150 where  $\mathbf{W}_f'$  denotes the conjugate transpose of  $\mathbf{W}_f$ ;  $\mathbf{\Lambda}_f \in \mathbb{R}^{N \times N}$  is the diagonal matrix of the  
 151 eigenvalues ( $\lambda_{i,f}^2 \in \mathbb{R}_+, i = 1, \dots, N$ ) and  $\mathbf{U}_f \in \mathbb{C}^{N \times N}$  is the matrix of column eigenvectors ( $\mathbf{u}_{i,f} \in$   
 152  $\mathbb{C}^N, i = 1, \dots, N$ ) of  $\mathbf{S}_f$ , respectively. We note here that  $\text{tr}(\mathbf{\Lambda}_f) = \text{tr}(\mathbf{S}_f)$ . If the interest is in  
 153 extracting modes which span a desired frequency band,  $\mathbf{S}_f$  can be integrated over that frequency  
 154 band before performing the eigen-decomposition. Here we define the MJO band-integrated ( $4 \leq$   
 155  $f \leq 12$  cpy) CSM as:

$$\mathbf{S}_{\text{MJO}} = \int_4^{12} \frac{\mathbf{S}_f}{f} df \in \mathbb{C}^{N \times N} \quad (3)$$

156 The diagonal matrix of eigenvalues and the matrix of column eigenvector of  $\mathbf{S}_{\text{MJO}}$  are  
 157  $\mathbf{\Lambda}_{\text{MJO}} = \text{diag}(\lambda_{i,\text{MJO}}^2 \in \mathbb{R}_+, i = 1, \dots, N) \in \mathbb{R}^{N \times N}$  and  $\mathbf{U}_{\text{MJO}} = (\mathbf{u}_{i,\text{MJO}} \in \mathbb{C}^N, i = 1, \dots, N) \in \mathbb{C}^{N \times N}$ ,  
 158 respectively. For unique solution of the eigen-decomposition in  $\mathbb{C}^{N \times N}$ , we impose unit L2-norm  
 159 for each eigenvector and a zero argument to the scalar element with the largest modulus in each  
 160 eigenvector. The wPC series of wavelet coefficients associated with the eigenvector  $\mathbf{u}_{i,\text{MJO}}$  at  
 161 frequency  $f$  is calculated as:

$$\boldsymbol{\kappa}_{i,f} = \mathbf{W}_f' \mathbf{u}_{i,\text{MJO}} \in \mathbb{C}^L \quad (4)$$

162 and the MJO band-integrated complex wPC series is then defined as:

$$\boldsymbol{\kappa}_{i,\text{MJO}} = \int_4^{12} \frac{\boldsymbol{\kappa}_{i,f}}{f} df \in \mathbb{C}^L \quad (5)$$

163 By design, the wsPCA separates modes of variability having distinct frequency supports. The  
 164 eigenvectors are represented as maps of complex loading coefficients whose argument  
 165 characterizes the relative phase shift (i.e. time delays) of the wPC time series between different  
 166 geographical locations, allowing wsPCA to handle potential non-synchronicity between the time

167 series  $\mathbf{x}_i$  and propagation effects. The use of the Morlet wavelet in particular allows optimal time-  
168 frequency localization and insensitivity to linear trends (Guiloteau et al., 2020).

### 169 **2.3. MJO Diagnostics**

170 **Spectral energy within the MJO frequency band:** The energy distribution of the analyzed  
171 signal across frequencies is described by the wavelet power spectral density (PSD):

$$PSD(f) = \frac{f_0}{f} \times \frac{1}{N(L-1)} \sum_{n=1}^N \sum_{l=1}^L |w_n(f, t_l)|^2 = \frac{f_0}{f} \times \frac{tr(\mathbf{S}_f)}{N} \quad (6)$$

172 and the energy contained within the MJO frequency band is given by:

$$\overline{PSD}_{\text{MJO}} = \frac{1}{12-4} \int_4^{12} PSD(f) df \quad (7)$$

173 The fraction of spectral power (FSP) contributed by the first wPC at frequency  $f$  is:

$$FSP_1(f) = \frac{\lambda_{1,f}^2}{tr(\mathbf{\Lambda}_f)} \quad (8)$$

174 and over the MJO frequency band is:

$$\overline{FSP}_{1,\text{MJO}} = \frac{\lambda_{1,\text{MJO}}^2}{tr(\mathbf{\Lambda}_{\text{MJO}})} \quad (9)$$

175 By comparing  $PSD(f)$ ,  $\overline{PSD}_{\text{MJO}}$ , and  $FSP_1(f)$ ,  $\overline{FSP}_{1,\text{MJO}}$  computed from observations and CMIP6  
176 model outputs, an assessment can be made of the ability of CMIP6 models to reproduce the total  
177 variance within intra-seasonal time scales and to model the MJO mode with the right contribution  
178 to the total intra-seasonal variance.

179 **Patterns and propagation speed of MJO:** Unlike classical PCA for which two  
180 eigenvectors and corresponding PCs are needed to capture the MJO (Wheeler & Hendon, 2004),  
181 for wsPCA only the first complex eigenvector  $\mathbf{u}_{1,\text{MJO}}$  and the first complex wPC series  $\mathbf{\kappa}_{1,\text{MJO}}$  are  
182 needed. Specifically, the maps of  $|\mathbf{u}_{1,\text{MJO}}|$  and  $arg(\mathbf{u}_{1,\text{MJO}})$  capture the magnitude and phase,  
183 respectively, of the MJO pattern. To compare MJO patterns between observations and models, the  
184 complex correlation coefficient is calculated as:

$$\rho^{\mathbf{u}_{1,\text{MJO}}} = \frac{\mathbf{u}_{1,\text{MJO}}^{\text{obs}} \cdot \mathbf{u}_{1,\text{MJO}}^{*\text{mod}}}{|\mathbf{u}_{1,\text{MJO}}^{\text{obs}}|_2 \cdot |\mathbf{u}_{1,\text{MJO}}^{*\text{mod}}|_2} \in \mathbb{C} \quad (10)$$

185 where  $\mathbf{u}^*$  is the complex conjugate and  $|\mathbf{u}|_2$  is the L2-norm of  $\mathbf{u}$ , respectively.

186 The wPC1 series  $\mathbf{\kappa}_{1,\text{MJO}}$  is used to quantitatively diagnose the magnitude and propagation  
187 dynamics of MJO. In the two-dimensional complex space defined by the real and imaginary parts  
188 of  $\mathbf{\kappa}_{1,\text{MJO}}$ , we form a wsPCA MJO index akin to the previous indices (Kiladis et al., 2014; Wheeler  
189 & Hendon, 2004). Based on the variable used (i.e. OLR or PPT), we designate this index as the  
190 wsPCA-based OLR MJO index (wOMI) or the wsPCA-based PPT MJO index (wPMI),  
191 respectively. To allow comparison between models and observations, the wPC1 series ( $\mathbf{\kappa}_{1,\text{MJO}}$ ) of

192 each model are normalized by the standard deviation of that obtained from observations.  
 193 Specifically, we work with:

$$\hat{\kappa}_{1,\text{MJO}} = \frac{\kappa_{1,\text{MJO}}}{\lambda_{1,\text{MJO}}^{\text{obs}}/\sqrt{2}} \in \mathbb{C}^L \quad (11)$$

194 Note here that  $\lambda_{1,\text{MJO}}^{\text{obs}} = \sqrt{2}\sigma_{\Re(\kappa_{1,\text{MJO}}^{\text{obs}})} = \sqrt{2}\sigma_{\Im(\kappa_{1,\text{MJO}}^{\text{obs}})}$ . At any time  $t$ , the modulus and argument of  
 195  $\hat{\kappa}_{1,\text{MJO}}(t)$  define the instantaneous intensity and phase of the MJO, respectively. Since  
 196  $\arg(\hat{\kappa}_{1,\text{MJO}}(t)) \in [0, 2\pi]$ , the eight traditional phases of MJO correspond to angular sectors each  
 197 spanning over  $\frac{\pi}{4}$  radians in the complex plane. The angular frequency  $\omega_{1,\text{MJO}}(t) =$   
 198  $\Delta\arg(\hat{\kappa}_{1,\text{MJO}}(t))/\Delta t$  represents the instantaneous propagation speed of MJO. In the rest of the  
 199 paper, we only discuss wOMI as the primary MJO index as we will show later that the MJO pattern  
 200 is reproduced more accurately by models using OLR than PPT.

201 In order to compare models to observations in term of their ability to capture both the  
 202 magnitude and instantaneous propagating speed of MJO, we form the bivariate probability density  
 203 function (PDF) of  $|\hat{\kappa}_{1,\text{MJO}}(t)|$  and  $\omega_{1,\text{MJO}}(t)$  for models and observations and compare them using  
 204 a distance metric. We choose the Wasserstein (or Earth Mover's) distance (WD) (Kantorovich,  
 205 2006; Rubner et al., 2000) which is a nonlinear metric defined as the minimal amount of work, or  
 206 optimal mass transport (Villani, 2008), needed to transform a discrete probability distribution to  
 207 another. This metric allows to rank CMIP6 models based on their skill to reproduce the magnitude  
 208 and dynamics of MJO.

### 209 3. Results

210 Figure 1 (a1,b1 – top row) shows the power spectral density (PSD) of PPT and OLR for  
 211 the observations, reanalysis, and 20 CMIP6 models. The PSD indicates that much of the energy of  
 212 both variables is concentrated within the ENSO timescale (2-7 years), highlighting the dominant  
 213 influence of this interannual variability mode on the climate system. At intra-seasonal timescales  
 214 (1-3 months), the PSD obtained from the multi-model ensemble (MME) mean of PPT is  
 215 comparable to that from the observations, whereas the PSD of OLR in CMIP6 models is generally  
 216 higher than that of observations and reanalysis.

217 The fraction of power spectra contributed by wPC1 ( $FPS_1$ ) is presented in Figure 1 (a2,b2  
 218 – bottom row). We note that  $FPS_1$  is high at low-frequencies (interannual and lower frequencies)  
 219 for both PPT and OLR (40-70% of the spectral power is contributed by wPC1 within the ENSO  
 220 timescale). At intra-seasonal timescales, the  $FPS_1$  of OLR ranges from 4-18% and that of PPT is  
 221 slightly lower. Nevertheless, while the observations and reanalysis show a well-defined peak in  
 222  $FPS_1$  within the MJO timescale (reaching up to 18%) indicating a coherent signal of MJO (inset  
 223 plots), many models substantially underestimate  $FPS_1$  within the MJO timescale and show no  
 224 well-defined peak. This result implies that, although CMIP6 models do not lack total variance  
 225 within intra-seasonal timescales (Figure 1 – top panels), they fail to properly model the MJO mode  
 226 of variability. Comparisons of the PSD and  $FPS_1$  among observed precipitation products are  
 227 further shown in Figure S1.

228 The spatial pattern of  $|\mathbf{u}_{1,\text{MJO}}|$  computed from observed OLR shows a coherent spatio-  
 229 temporal mode spanning from the tropical Indian Ocean to the Western Pacific (Figure 2a) and the  
 230 pattern of  $\arg(\mathbf{u}_{1,\text{MJO}})$  shown in Figure 2b clearly indicates eastward propagation of MJO,

231 demonstrating the robustness of the wsPCA to identify the MJO as the dominant mode in the 4-12  
 232 cpy frequency band. The spatial patterns of the magnitude and argument of  $\mathbf{u}_{1,\text{MJO}}$  of OLR and  
 233 PPT for all CMIP6 models, reanalysis, and observations are presented in Figures S2-S5 for  
 234 comparison. Furthermore, the lag-longitude diagrams of the reconstructed OLR and PPT  
 235 anomalies within the MJO timescale are shown in Figure S6. It can be seen that the average  
 236 eastward propagation speed of MJO as estimated from the observations, reanalysis, and a large  
 237 number (13/20) of the models is about 5 m/s. Our results suggest that the majority of CMIP6  
 238 models are able to capture well the average propagation speed of MJO which is consistent with  
 239 previous studies (Ahn et al., 2020; Orbe et al., 2020). Nevertheless, many models underestimate  
 240 the MJO variability as reflected by the lower values of the normalized magnitudes  
 241  $\frac{\lambda_{1,\text{MJO}} \times \sqrt{N}}{\sqrt{\text{tr}(\Lambda_{\text{MJO}})}} |\mathbf{u}_{1,\text{MJO}}|$  compared to those of the observations (Figures S2&S4). Moreover, the  
 242 magnitude of the wPC1 time series  $\kappa_{1,f}$  across frequencies is presented in Figure 2c, showing  
 243 considerable interannual variability in MJO activity. Figure 2d shows the trajectory in the complex  
 244 plane of the daily wOMI obtained from observations during the study period. The trajectories of  
 245 daily wOMI and wPMI obtained from all datasets are further presented in Figures S7-S8.

246 Comparison of the  $\overline{PSD}_{\text{MJO}}$  and  $\overline{FSP}_{1,\text{MJO}}$  for PPT and OLR is shown in Figure 3a-b,  
 247 respectively. For PPT, while the CMIP6 models show a spread of the  $\overline{PSD}_{\text{MJO}}$  above and below  
 248 the value of the observations indicating no systematic bias, the  $\overline{FSP}_{1,\text{MJO}}$  estimated from the  
 249 models is consistently smaller than that from the observations, indicating that the models  
 250 systematically underestimate the MJO variability. For OLR, most CMIP6 models exhibit higher  
 251  $\overline{PSD}_{\text{MJO}}$  than observations (except model IPSL-CM6A-LR(13); Figure 3b); however all models  
 252 show lower  $\overline{FSP}_{1,\text{MJO}}$  than that of the observations, further confirming that CMIP6 models  
 253 consistently underestimate the contribution of the MJO to intra-seasonal climate variability. For  
 254 both variables,  $\overline{PSD}_{\text{MJO}}$  of the reanalysis is slightly higher than in the observations, but the  
 255  $\overline{FSP}_{1,\text{MJO}}$  is lower. The scatter plot of the modulus of the complex pattern correlation coefficients  
 256  $|\rho_{\text{OLR}}^{u_{1,\text{MJO}}}|$  and  $|\rho_{\text{PPT}}^{u_{1,\text{MJO}}}|$  as defined in Equation (10) is shown in Figure 3c. Most of the models show  
 257 correlations in the range of 0.6-0.85 for both variables, confirming that, for all models, the first  
 258 dynamical mode extracted by the wsPCA in the 4-12 cpy frequency band is actually the MJO, and  
 259 indicating quite good agreement of the modeled MJO patterns to the observed ones. We note  
 260 however that the complex pattern correlation only indicates agreement between the unit-norm first  
 261 complex eigenvectors (Equation 10) and does not take into account the discrepancy between their  
 262 corresponding eigenvalues (variance explained), a discrepancy that has been separately assessed  
 263 in Figure 3a-b. Two models showing very low values of  $|\rho_{\text{OLR}}^{u_{1,\text{MJO}}}|$  and  $|\rho_{\text{PPT}}^{u_{1,\text{MJO}}}|$  are the IPSL-  
 264 CM6A-LR(13) and CanEMS(5). Finally, most of the scatter points are below the 1:1 line,  
 265 implying that CMIP6 models generally reproduce more accurately the patterns of OLR than PPT.

266 Figure 4a compares the relationship of the magnitude and propagation speed of MJO for  
 267 models, reanalysis, and observations for all days during 1983-2014 (these can be seen as joint  
 268 PDFs). Note that the normalized wPC series  $\hat{\kappa}_{1,\text{MJO}}$  (see Section 2.3) are plotted to allow  
 269 comparison between models and observations. We find that while the average propagation speed  
 270 (mean of the PDF of  $\omega_{1,\text{MJO}}(t)$ ) is quite similar among all models (0.1 – 0.13 rad/day, equivalent  
 271 cycles of 60 – 48 days), CMIP6 models underestimate the magnitude  $|\hat{\kappa}_{1,\text{MJO}}|$  of the MJO mode.  
 272 The marginal PDFs of  $|\hat{\kappa}_{1,\text{MJO}}(t)|$  and  $\omega_{1,\text{MJO}}(t)$  for all datasets are shown in Figure 4b further

273 demonstrating that most of CMIP6 models capture the MJO propagation speed but underestimate  
 274 the amplitude of MJO compared to the observations (as also shown in Figure 4a). Moreover,  
 275 Figure 4c shows the ranked WD between the joint PDFs of  $|\hat{\kappa}_{1,MJO}(t)|$  and  $\omega_{1,MJO}(t)$  inferred by  
 276 the observations (reference) and those obtained from the reanalysis (red bar) and CMIP6 models  
 277 (grey bars). The smaller the values of the WD, the better the performance of a model to reproduce  
 278 the observed MJO magnitude and speed. Relatively good models that show the smallest WD values  
 279 include the NESM3(19) and SAM0-UNICON(20) that are consistent with recent reports on the  
 280 improvements of MJO simulations in these models (Shin & Park, 2020; Yang et al., 2020).

281 In Figure 5, we evaluate the impact of the MJO on precipitation over the Amazonia,  
 282 Southwest Africa, and Maritime Continent regions. The Hovmöller phase-longitude diagrams of  
 283 PPT anomalies show that the MME mean produces smaller MJO-related precipitation variability  
 284 compared to the observations during all eight MJO phases and in all regions (Figure 5a). Details  
 285 of the Hovmöller diagrams for each model in each region are further shown in Figures S9-S11.  
 286 These diagrams suggest that a large number of CMIP6 models underestimate the MJO signal to  
 287 regional precipitation compared to the observations. Among the three regions, the models produce  
 288 the most realistic precipitation variability in the Maritime Continent where MJO activity is the  
 289 greatest. Furthermore, the scatter plots of the WD and correlation coefficients of the Hovmöller  
 290 diagrams of PPT ( $\rho_{PPT}^{Hov}$ ) between models and observations for each region are presented in  
 291 Figure 5b-d. It can be seen that models showing good performance in reproducing the MJO  
 292 magnitude (i.e. models with low WD value) also tend to exhibit higher correlation of  $\rho_{PPT}^{Hov}$  with  
 293 observations and larger MJO-related precipitation variability in the Amazonia and Maritime  
 294 Continent, while this tendency is not observed in Southwestern Africa. Our results suggest that  
 295 CMIP6 models which underestimate MJO magnitude also reproduce weak MJO teleconnections  
 296 to regional precipitation.

#### 297 4. Conclusions

298 In this study, we have analyzed historical simulations of 20 CMIP6 models to assess their  
 299 ability to capture the space-time dynamics of MJO. For the first time, we applied the wsPCA to  
 300 extract the pattern, magnitude, and eastward propagation of MJO from daily PPT and OLR. The  
 301 key advantage of wsPCA compared to other PCA methods is that the cross-spectral matrix (CSM)  
 302 between time series across locations is estimated using a complex CWT enabling robust estimation  
 303 of the CSM in any desired frequency band. Moreover, the wsPCA is non-parametric and simple to  
 304 implement compared to nonlinear dimensionality reduction approaches, such as the nonlinear  
 305 Laplacian spectral analysis (NLSA) (Giannakis & Majda, 2012), which significantly facilitates the  
 306 extraction of dynamical modes from a large number of models. We defined the wsPCA MJO  
 307 indices (wOMI and wMPI) based on the real and imaginary parts of the MJO band-integrated (4-  
 308 12 cpy) complex wPC1 series to evaluate the magnitude and phase of the MJO mode at the daily  
 309 scale and compare models with observations. We then investigated the influence of MJO to  
 310 precipitation variability in CMIP6 models over three different regions.

311 The analysis herein showed that most CMIP6 models are able to realistically capture the  
 312 eastward propagation of MJO as also reported in recent studies (Ahn et al., 2020; Orbe et al.,  
 313 2020). However, the simulation of the MJO magnitude in CMIP6 remains a challenging problem.  
 314 We demonstrated that although CMIP6 models exhibit enough spectral power or total variance  
 315 within the intra-seasonal timescales as compared to observations, they tend to underestimate the  
 316 variability contributed by the MJO mode. Furthermore, we showed that precipitation variability

317 associated with the MJO is underestimated in the CMIP6 models in the Amazonia, Southwest  
 318 Africa and Maritime Continent. Our results highlight the need to better simulate the coupled ocean-  
 319 atmosphere dynamics in climate models to improve the MJO representation and MJO-driven  
 320 tropical and extratropical rainfall.

## 321 **Acknowledgments, Samples, and Data**

322 The authors acknowledge support provided by the National Science Foundation (NSF)  
 323 under the TRIPODS+X program (grant DMS-1839336) and the EAGER program (grant ECCS-  
 324 1839441), as well as by NASA's Global Precipitation Measurement program (grant  
 325 80NSSC19K0684). Upon request, the code that supports the findings of this paper can be provided  
 326 by the corresponding authors.

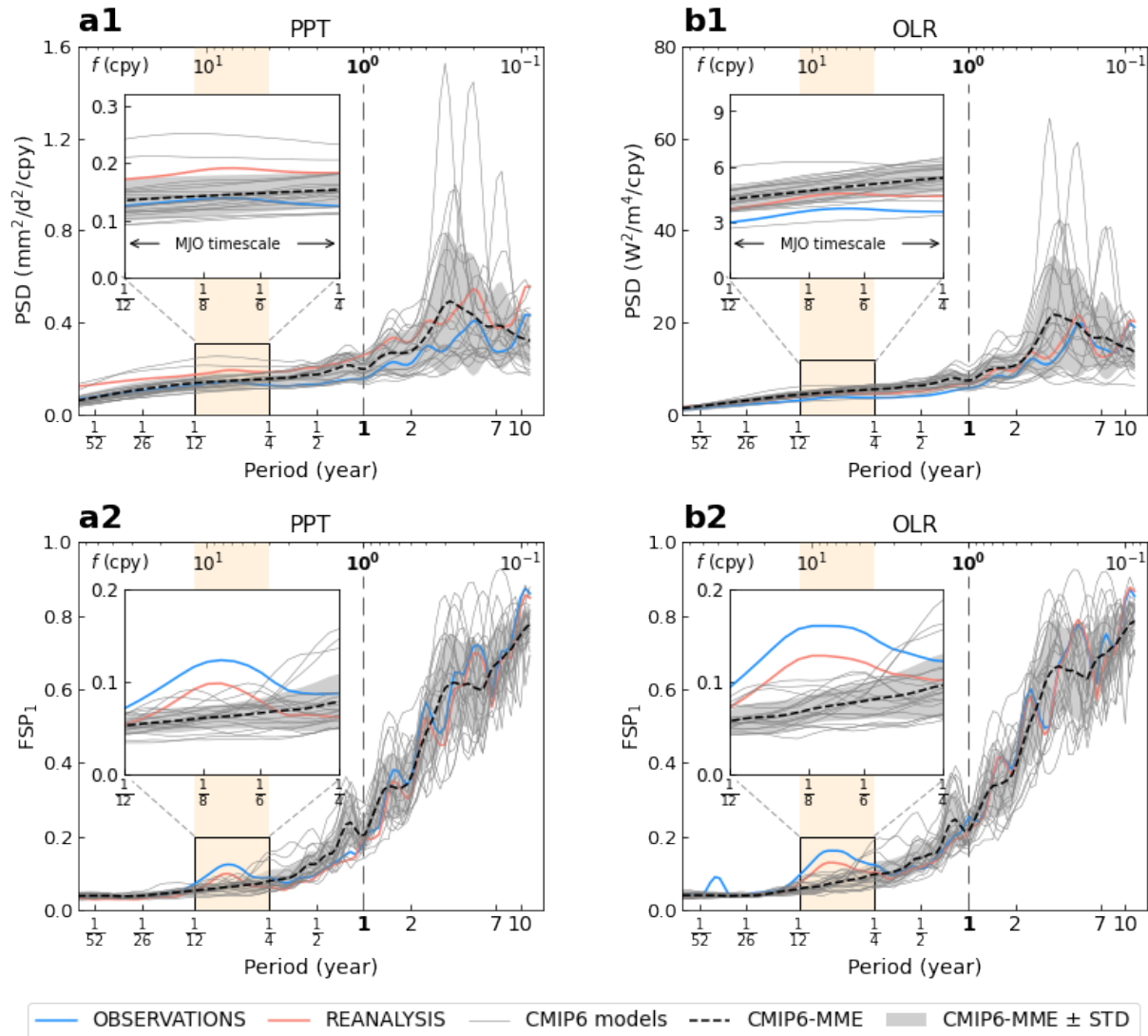
327 The authors acknowledge the FAIR data policy. The CMIP6 data set is available at  
 328 <https://esgf-node.llnl.gov/projects/cmip6>. The ECMWF ERA5 reanalysis data set was downloaded  
 329 from <https://www.ecmwf.int/en/forecasts/datasets/reanalysis-datasets/era5>. The PERSIANN-  
 330 CDR precipitation data was downloaded from <https://chrsdata.eng.uci.edu/>. The interpolated OLR  
 331 data of NCAR and the GPCP v2.3 precipitation data were provided by the NOAA/ESRL PSD,  
 332 Boulder, CO, USA (<https://psl.noaa.gov/data/gridded/index.html>). The TRMM (34B2) and  
 333 IMERG precipitation data were provided by the NASA's Precipitation Measurement Missions  
 334 (<https://gpm.nasa.gov/data/directory>). The CMORPH precipitation data was provided by the  
 335 NOAA/CPC ([https://www.cpc.ncep.noaa.gov/products/janowiak/cmorph\\_description.html](https://www.cpc.ncep.noaa.gov/products/janowiak/cmorph_description.html)).  
 336

## 337 **References**

- 338 Addison, P. S. (2002). *The Illustrated Wavelet Transform Handbook: Introductory Theory and Applications in*  
 339 *Science, Engineering, Medicine and Finance*: Taylor & Francis.
- 340 Ahn, M.-S., Kim, D., Kang, D., Lee, J., Sperber, K. R., Gleckler, P. J., et al. (2020). MJO Propagation Across the  
 341 Maritime Continent: Are CMIP6 Models Better Than CMIP5 Models? *Geophysical Research Letters*,  
 342 47(11), e2020GL087250.
- 343 Ahn, M.-S., Kim, D., Sperber, K. R., Kang, I.-S., Maloney, E., Waliser, D., et al. (2017). MJO simulation in CMIP5  
 344 climate models: MJO skill metrics and process-oriented diagnosis. *Climate Dynamics*, 49(11), 4023-4045.
- 345 Ashouri, H., Hsu, K.-L., Sorooshian, S., Braithwaite, D. K., Knapp, K. R., Cecil, L. D., et al. (2015). PERSIANN-  
 346 CDR: Daily Precipitation Climate Data Record from Multisatellite Observations for Hydrological and  
 347 Climate Studies. *Bulletin of the American Meteorological Society*, 96(1), 69-83.
- 348 Bessafi, M., & Wheeler, M. C. (2006). Modulation of South Indian Ocean Tropical Cyclones by the Madden-Julian  
 349 Oscillation and Convectively Coupled Equatorial Waves. *Monthly Weather Review*, 134(2), 638-656.  
 350 <https://doi.org/10.1175/MWR3087.1>
- 351 Brodzik, M. J., Billingsley, B., Haran, T., Raup, B., & Savoie, M. H. (2014). Correction: Brodzik, M.J., et al. EASE-  
 352 Grid 2.0: Incremental but Significant Improvements for Earth-Gridded Data Sets. *ISPRS International*  
 353 *Journal of Geo-Information* 2012, 1, 32–45. *ISPRS International Journal of Geo-Information*, 3(3), 1154-  
 354 1156.
- 355 Eyring, V., Bony, S., Meehl, G. A., Senior, C. A., Stevens, B., Stouffer, R. J., & Taylor, K. E. (2016). Overview of  
 356 the Coupled Model Intercomparison Project Phase 6 (CMIP6) experimental design and organization.  
 357 *Geoscientific Model Development*, 9(5), 1937-1958.
- 358 Eyring, V., Cox, P. M., Flato, G. M., Gleckler, P. J., Abramowitz, G., Caldwell, P., et al. (2019). Taking climate  
 359 model evaluation to the next level. *Nature Climate Change*, 9(2), 102-110.
- 360 Giannakis, D., & Majda, A. J. (2012). Nonlinear Laplacian spectral analysis for time series with intermittency and  
 361 low-frequency variability. *Proceedings of the National Academy of Sciences*, 109(7), 2222-2227.  
 362 <https://www.pnas.org/content/pnas/109/7/2222.full.pdf>
- 363 Guilloteau, C., Mamalakis, A., Vulis, L., Le, P. V. V., Georgiou, T. T., & Foufoula-Georgiou, E. (2020). Rotated  
 364 spectral principal component analysis (rsPCA) for identifying dynamical modes of variability in climate  
 365 systems. *Journal of Climate*, 1-59. <https://doi.org/10.1175/JCLI-D-20-0266.1>

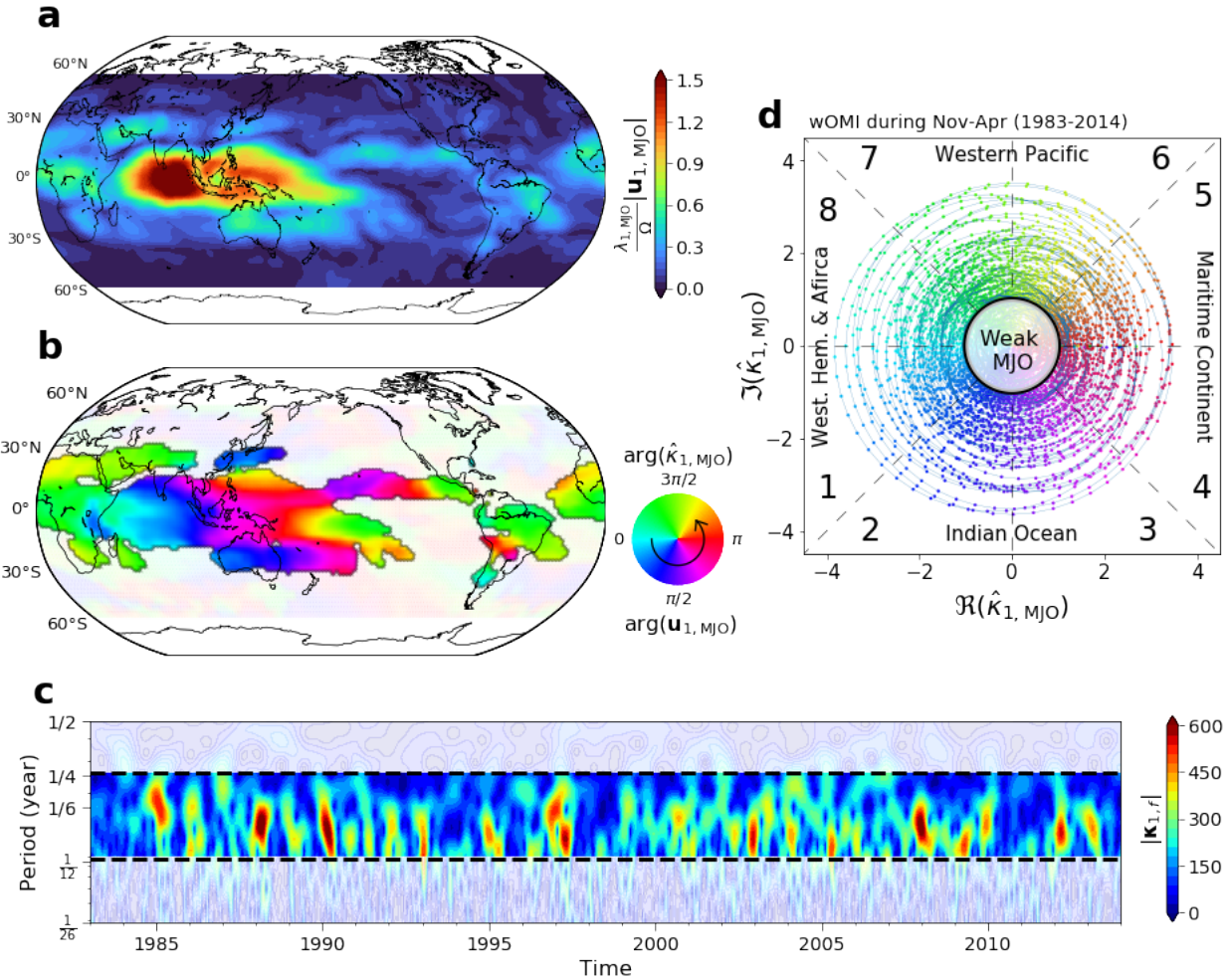
- 366 Hannachi, A., Jolliffe, I. T., & Stephenson, D. B. (2007). Empirical orthogonal functions and related techniques in  
367 atmospheric science: A review. *International Journal of Climatology*, 27(9), 1119-1152.
- 368 Hendon, H. H., & Wheeler, M. C. (2008). Some Space–Time Spectral Analyses of Tropical Convection and  
369 Planetary-Scale Waves. *Journal of the Atmospheric Sciences*, 65(9), 2936-2948.  
370 <https://doi.org/10.1175/2008JAS2675.1>
- 371 Hendon, H. H., Wheeler, M. C., & Zhang, C. (2007). Seasonal Dependence of the MJO–ENSO Relationship.  
372 *Journal of Climate*, 20(3), 531-543. <https://doi.org/10.1175/JCLI4003.1>
- 373 Hersbach, H., Bell, B., Berrisford, P., Hirahara, S., Horányi, A., Muñoz-Sabater, J., et al. (2020). The ERA5 global  
374 reanalysis. *Quarterly Journal of the Royal Meteorological Society*, 146(730), 1999-2049.
- 375 Hung, M.-P., Lin, J.-L., Wang, W., Kim, D., Shinoda, T., & Weaver, S. J. (2013). MJO and Convectively Coupled  
376 Equatorial Waves Simulated by CMIP5 Climate Models. *Journal of Climate*, 26(17), 6185-6214.
- 377 Jiang, X., Adames, Á. F., Kim, D., Maloney, E. D., Lin, H., Kim, H., et al. (2020). Fifty Years of Research on the  
378 Madden-Julian Oscillation: Recent Progress, Challenges, and Perspectives. *Journal of Geophysical*  
379 *Research: Atmospheres*, 125(17), e2019JD030911. <https://doi.org/10.1029/2019JD030911>.  
380 <https://doi.org/10.1029/2019JD030911>
- 381 Jiang, X., Waliser, D. E., Xavier, P. K., Petch, J., Klingaman, N. P., Woolnough, S. J., et al. (2015). Vertical  
382 structure and physical processes of the Madden-Julian oscillation: Exploring key model physics in climate  
383 simulations. *Journal of Geophysical Research: Atmospheres*, 120(10), 4718-4748.  
384 <https://agupubs.onlinelibrary.wiley.com/doi/abs/10.1002/2014JD022375>
- 385 Jones, C., Waliser, D. E., Lau, K. M., & Stern, W. (2004). Global Occurrences of Extreme Precipitation and the  
386 Madden–Julian Oscillation: Observations and Predictability. *Journal of Climate*, 17(23), 4575-4589.  
387 <https://doi.org/10.1175/3238.1>
- 388 Kantorovich, L. V. (2006). On the Translocation of Masses. *Journal of Mathematical Sciences*, 133(4), 1381-1382.  
389 <https://doi.org/10.1007/s10958-006-0049-2>
- 390 Kiladis, G. N., Dias, J., Straub, K. H., Wheeler, M. C., Tulich, S. N., Kikuchi, K., et al. (2014). A Comparison of  
391 OLR and Circulation-Based Indices for Tracking the MJO. *Monthly Weather Review*, 142(5), 1697-1715.  
392 <https://doi.org/10.1175/MWR-D-13-00301.1>
- 393 Kiladis, G. N., Straub, K. H., & Haertel, P. T. (2005). Zonal and Vertical Structure of the Madden–Julian  
394 Oscillation. *Journal of the Atmospheric Sciences*, 62(8), 2790-2809.
- 395 Kim, H., Caron, J. M., Richter, J. H., & Simpson, I. R. (2020). The Lack of QBO-MJO Connection in CMIP6  
396 Models. *Geophysical Research Letters*, 47(11), e2020GL087295.  
397 <https://agupubs.onlinelibrary.wiley.com/doi/abs/10.1029/2020GL087295>
- 398 Klotzbach, P. J. (2010). On the Madden–Julian Oscillation–Atlantic Hurricane Relationship. *Journal of Climate*,  
399 23(2), 282-293. <https://doi.org/10.1175/2009JCLI2978.1>
- 400 Lambert, S. J., & Boer, G. J. (2001). CMIP1 evaluation and intercomparison of coupled climate models. *Climate*  
401 *Dynamics*, 17(2), 83-106.
- 402 Lau, W. K., & Waliser, D. E. (2012). El Niño southern oscillation connection. In *Intraseasonal Variability in the*  
403 *Atmosphere–Ocean Climate System* (pp. 297-334): Springer.
- 404 Lin, J.-L., Kiladis, G. N., Mapes, B. E., Weickmann, K. M., Sperber, K. R., Lin, W., et al. (2006). Tropical  
405 Intraseasonal Variability in 14 IPCC AR4 Climate Models. Part I: Convective Signals. *Journal of Climate*,  
406 19(12), 2665-2690. <https://doi.org/10.1175/JCLI3735.1>
- 407 Lo, F., & Hendon, H. H. (2000). Empirical Extended-Range Prediction of the Madden–Julian Oscillation. *Monthly*  
408 *Weather Review*, 128(7), 2528-2543. [https://doi.org/10.1175/1520-0493\(2000\)128<2528:EERPOT>2.0.CO;2](https://doi.org/10.1175/1520-0493(2000)128<2528:EERPOT>2.0.CO;2)
- 409 Lorenz, D. J., & Hartmann, D. L. (2006). The Effect of the MJO on the North American Monsoon\*. *Journal of*  
410 *Climate*, 19(3), 333-343. <https://doi.org/10.1175/JCLI3684.1>
- 411 Madden, R. A., & Julian, P. R. (1971). Detection of a 40–50 Day Oscillation in the Zonal Wind in the Tropical  
412 Pacific. *Journal of the Atmospheric Sciences*, 28(5), 702-708.
- 413 Madden, R. A., & Julian, P. R. (1972). Description of Global-Scale Circulation Cells in the Tropics with a 40–50  
414 Day Period. *Journal of the Atmospheric Sciences*, 29(6), 1109-1123.
- 415 Maloney, E. D., & Hartmann, D. L. (1998). Frictional Moisture Convergence in a Composite Life Cycle of the  
416 Madden–Julian Oscillation. *Journal of Climate*, 11(9), 2387-2403. [https://doi.org/10.1175/1520-0442\(1998\)011<2387:FMCIAC>2.0.CO;2](https://doi.org/10.1175/1520-0442(1998)011<2387:FMCIAC>2.0.CO;2)
- 417 Maloney, E. D., & Hartmann, D. L. (2000). Modulation of Hurricane Activity in the Gulf of Mexico by the Madden-  
418 Julian Oscillation. *Science*, 287(5460), 2002-2004.  
419 <https://science.sciencemag.org/content/sci/287/5460/2002.full.pdf>

- 422 Meehl, G. A., Covey, C., Delworth, T., Latif, M., McAvaney, B., Mitchell, J. F. B., et al. (2007). THE WCRP  
 423 CMIP3 Multimodel Dataset: A New Era in Climate Change Research. *Bulletin of the American*  
 424 *Meteorological Society*, 88(9), 1383-1394.
- 425 Meehl, G. A., Stocker, T. F., Collins, W. D., Friedlingstein, P., Gaye, A. T., Gregory, J. M., et al. (2007). Global  
 426 climate projections. In *Climate Change 2007: The physical science basis* (pp. 747-846). United Kingdom:  
 427 Cambridge University Press.
- 428 Orbe, C., Van Roekel, L., Adames, Á. F., Dezfuli, A., Fasullo, J., Gleckler, P. J., et al. (2020). Representation of  
 429 Modes of Variability in Six U.S. Climate Models. *Journal of Climate*, 33(17), 7591-7617.
- 430 Robertson, A. W., Kumar, A., Peña, M., & Vitart, F. (2015). Improving and Promoting Subseasonal to Seasonal  
 431 Prediction. *Bulletin of the American Meteorological Society*, 96(3), ES49-ES53.
- 432 Roxy, M. K., Dasgupta, P., McPhaden, M. J., Suematsu, T., Zhang, C., & Kim, D. (2019). Twofold expansion of the  
 433 Indo-Pacific warm pool warps the MJO life cycle. *Nature*, 575(7784), 647-651.  
 434 <https://doi.org/10.1038/s41586-019-1764-4>
- 435 Rubner, Y., Tomasi, C., & Guibas, L. J. (2000). The Earth Mover's Distance as a Metric for Image Retrieval.  
 436 *International Journal of Computer Vision*, 40(2), 99-121. <https://doi.org/10.1023/A:1026543900054>
- 437 Schmidt, O. T., Mengaldo, G., Balsamo, G., & Wedi, N. P. (2019). Spectral Empirical Orthogonal Function  
 438 Analysis of Weather and Climate Data. *Monthly Weather Review*, 147(8), 2979-2995.  
 439 <https://doi.org/10.1175/MWR-D-18-0337.1>
- 440 Shin, J., & Park, S. (2020). Impacts of ENSO and Madden–Julian oscillation on the genesis of tropical cyclones  
 441 simulated by general circulation models and compared to observations. *Environmental Research Letters*,  
 442 15(3), 034046. <http://dx.doi.org/10.1088/1748-9326/ab7466>
- 443 Takayabu, Y. N., Iguchi, T., Kachi, M., Shibata, A., & Kanzawa, H. (1999). Abrupt termination of the 1997–98 El  
 444 Niño in response to a Madden–Julian oscillation. *Nature*, 402(6759), 279-282.  
 445 <https://doi.org/10.1038/46254>
- 446 Taraphdar, S., Zhang, F., Leung, L. R., Chen, X., & Pauluis, O. M. (2018). MJO Affects the Monsoon Onset Timing  
 447 Over the Indian Region. *Geophysical Research Letters*, 45(18), 10011-10018.  
 448 <https://agupubs.onlinelibrary.wiley.com/doi/abs/10.1029/2018GL078804>
- 449 Taylor, K. E., Stouffer, R. J., & Meehl, G. A. (2012). An Overview of CMIP5 and the Experiment Design. *Bulletin*  
 450 *of the American Meteorological Society*, 93(4), 485-498.
- 451 Villani, C. (2008). *Optimal transport: old and new* (Vol. 338): Springer Science & Business Media.
- 452 Waliser, D. E., Lau, K. M., Stern, W., & Jones, C. (2003). Potential Predictability of the Madden–Julian Oscillation.  
 453 *Bulletin of the American Meteorological Society*, 84(1), 33-50. <https://doi.org/10.1175/BAMS-84-1-33>
- 454 Wheeler, M. C., & Hendon, H. H. (2004). An All-Season Real-Time Multivariate MJO Index: Development of an  
 455 Index for Monitoring and Prediction. *Monthly Weather Review*, 132(8), 1917-1932.
- 456 Wheeler, M. C., & Kiladis, G. N. (1999). Convectively Coupled Equatorial Waves: Analysis of Clouds and  
 457 Temperature in the Wavenumber–Frequency Domain. *Journal of the Atmospheric Sciences*, 56(3), 374-  
 458 399.
- 459 Woolnough, S. J. (2019). Chapter 5 - The Madden-Julian Oscillation. In A. W. Robertson & F. Vitart (Eds.), *Sub-*  
 460 *Seasonal to Seasonal Prediction* (pp. 93-117): Elsevier.
- 461 Yang, Y.-M., Wang, B., Cao, J., Ma, L., & Li, J. (2020). Improved historical simulation by enhancing moist  
 462 physical parameterizations in the climate system model NESM3.0. *Climate Dynamics*, 54(7), 3819-3840.  
 463 <https://doi.org/10.1007/s00382-020-05209-2>
- 464 Zhang, C. (2005). Madden-Julian Oscillation. *Reviews of Geophysics*, 43(2).
- 465 Zhang, C., Dong, M., Gualdi, S., Hendon, H. H., Maloney, E. D., Marshall, A., et al. (2006). Simulations of the  
 466 Madden–Julian oscillation in four pairs of coupled and uncoupled global models. *Climate Dynamics*, 27(6),  
 467 573-592. <https://doi.org/10.1007/s00382-006-0148-2>
- 468



469

470 **Figure 1.** (Top) Power spectral density of (a1) daily precipitation rate (PPT) and (b1) daily  
 471 outgoing longwave radiation (OLR). (Bottom) Fraction of spectral power explained by wPC1 for  
 472 (a2) PPT and (b2) OLR. Blue lines correspond to observations, red lines to reanalysis data, dashed  
 473 black lines correspond to the multi-model ensemble (MME) mean of 20 CMIP6 models, and the  
 474 grey shaded regions represent MME  $\pm$  standard deviation (here individual models are not  
 475 distinguished from one another). The MJO timescale (yellow shaded vertical bands) ranges from  
 476 1-3 months. Frequency  $f$  in cycles per year (cpy) is shown in the top horizontal axes.



477

478 **Figure 2.** (a-b) Spatial patterns of the MJO band-integrated complex eigenvector  $\mathbf{u}_{1, \text{MJO}}$  for  
 479 observed OLR for (a) modulus (magnitude) and (b) argument (phase). The modulus is shown for

480 the unit-norm eigenvector with a scaling factor  $\frac{\lambda_{1, \text{MJO}}}{\Omega}$ , with  $\Omega = \sqrt{\frac{\text{tr}(\Lambda_{\text{MJO}})}{N}}$ . The counter-

481 clockwise, circular arrow in the colorscale indicates the direction of the propagation of the

482 extracted wave. (c) Magnitude of the complex wavelet PC1 time series  $|\kappa_{1, f}|$  associated with

483  $\mathbf{u}_{1, \text{MJO}}$  across frequencies for observed OLR. (d) Trajectory in the complex plane of the wsPCA-

484 based OLR MJO index (wOMI)  $\hat{\kappa}_{1, \text{MJO}}$  for observed OLR. The wOMI is displayed during boreal

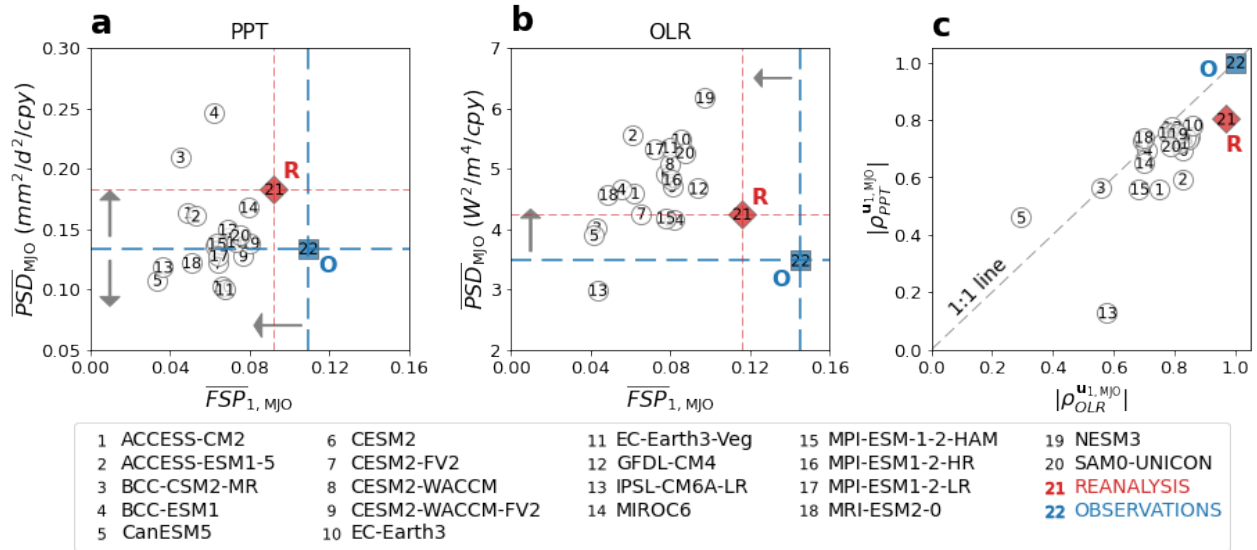
485 winter season (Nov-Apr) from 1983-2014 with one sample per day plotted. Points that lie inside

486 the black unit circle correspond to days that are classified as weak/inactive MJO. The same

487 colorscale as in panel (b) is used to represent the values of  $\arg(\hat{\kappa}_{1, \text{MJO}}(t))$ , indicating the

488 eastward propagation of MJO. See text for definition of variables.

489



490

491

492

493

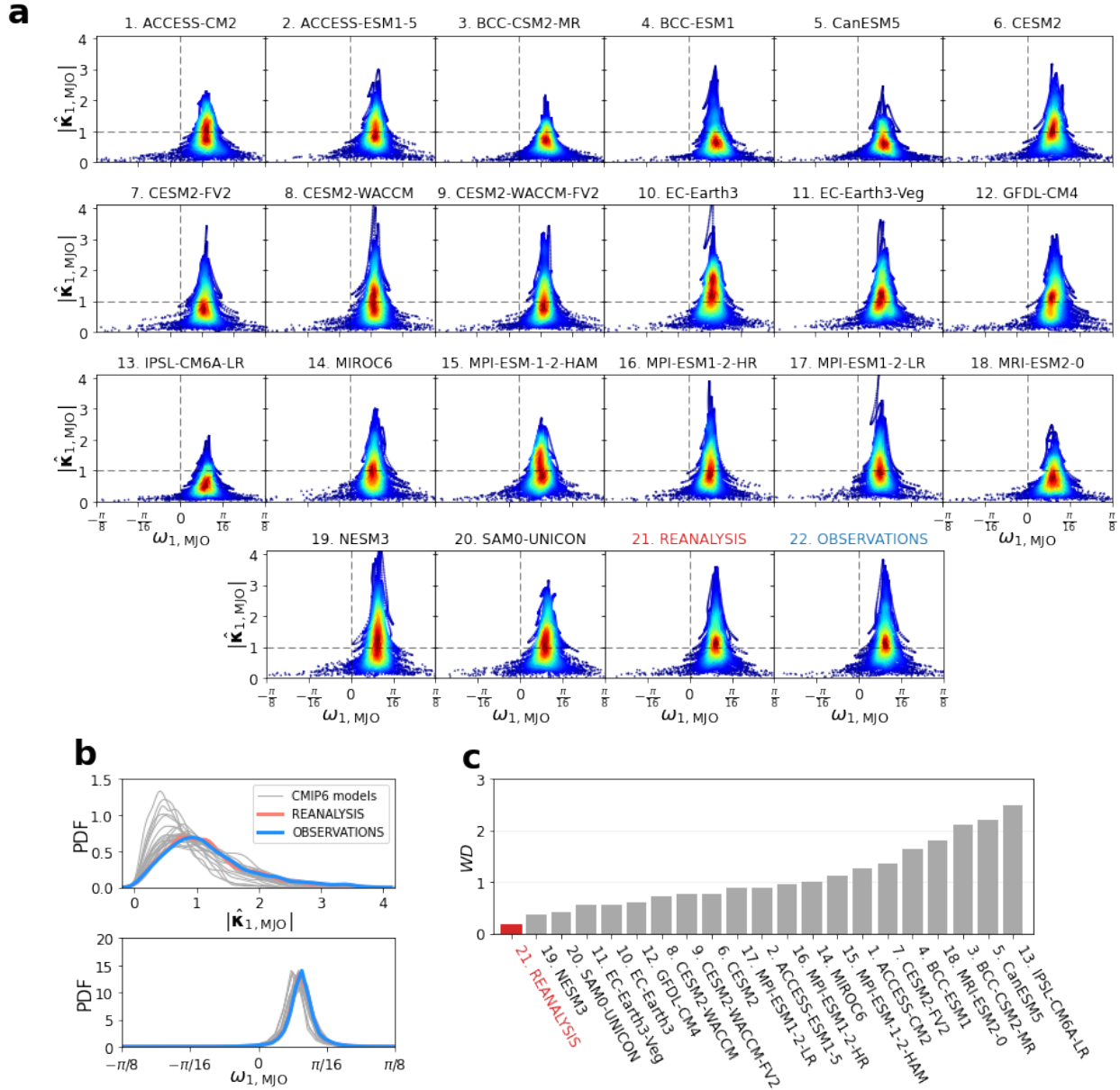
494

495

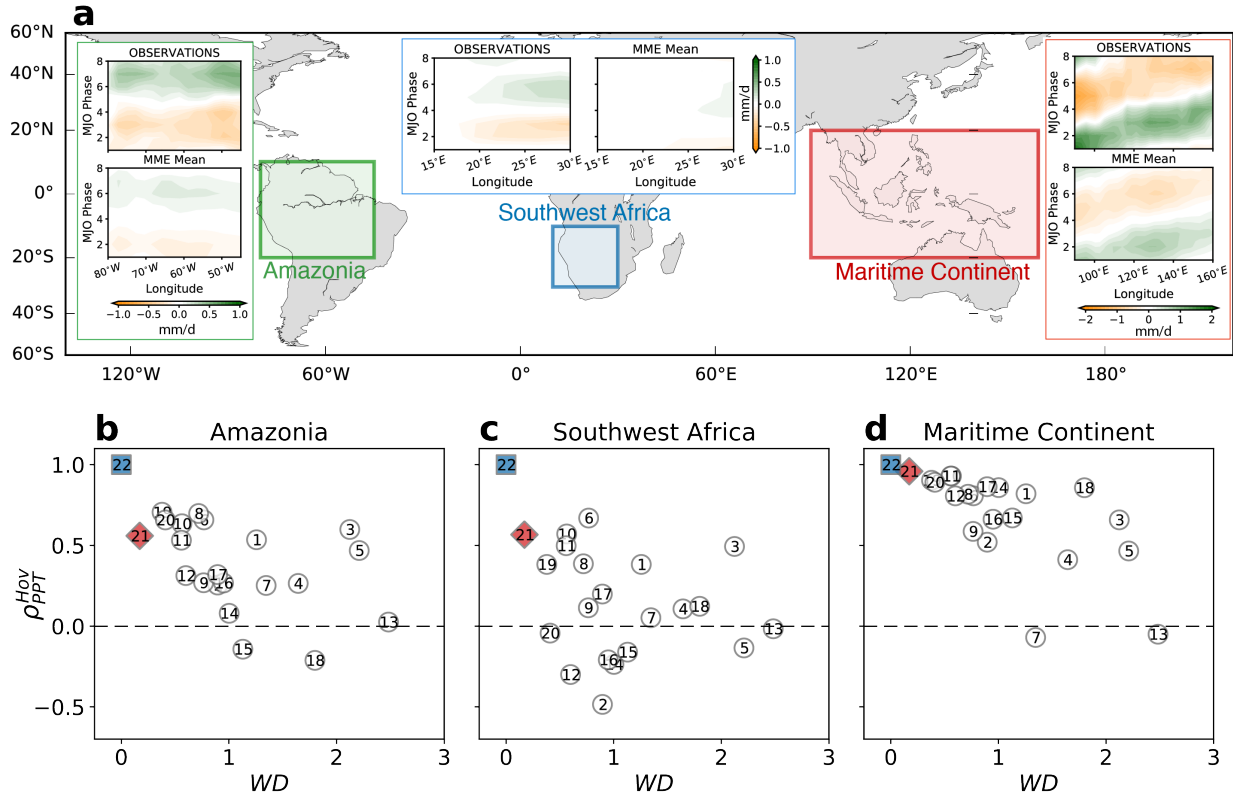
496

497

**Figure 3.** Comparison of spectral energy within the MJO frequency band ( $\overline{PSD}_{MJO}$ ) and the fraction of energy explained by wPC1 ( $\overline{FSP}_{1,MJO}$ ) for (a) Precipitation rate and (b) Outgoing longwave radiation for observations, reanalysis products and models. The systematic underestimation of  $\overline{FSP}_{1,MJO}$  in the models is apparent. (c) Scatter plot of the correlation coefficients of the patterns for the first complex eigenvectors of the modeled and observed OLR ( $|\rho_{OLR}^{u_{1,MJO}}|$ ) and modeled and observed PPT ( $|\rho_{PPT}^{u_{1,MJO}}|$ ) as defined in Equation (10). Numbers inside markers represent CMIP6 models (1-20), reanalysis (21), and observations (22).



498  
 499 **Figure 4.** (a) Relationship between the normalized magnitude  $|\hat{\kappa}_{1, \text{MJO}}(t)|$  and angular frequency  $\omega_{1, \text{MJO}}(t)$  of CMIP6 models, reanalysis products, and observations computed at the daily scale.  
 500 Points under the unit horizontal dashed lines are classified as weak MJO. The color scale  
 501 represents the joint PDF of  $|\hat{\kappa}_{1, \text{MJO}}(t)|$  and  $\omega_{1, \text{MJO}}(t)$ , with warmer color indicating higher  
 502 probability. (b) Probability density functions of the MJO band-integrated wPC1 series for (top)  
 503 magnitude  $|\hat{\kappa}_{1, \text{MJO}}(t)|$  and (bottom) angular frequency  $\omega_{1, \text{MJO}}(t)$ . (c) Wasserstein distance (WD)  
 504 between the joint probability distribution of  $|\hat{\kappa}_{1, \text{MJO}}(t)|$  and  $\omega_{1, \text{MJO}}(t)$  obtained from  
 505 observations (reference) and those obtained from reanalysis (red bar) and CMIP6 models (grey  
 506 bars). The WD values of models are sorted from low to high, indicating the ranking of CMIP6  
 507 models in reproducing the MJO magnitude and propagation dynamics.  
 508



509  
 510 **Figure 5. (a, Top)** Comparison of modeled (CMIP6 MME Mean) and observed MJO-related  
 511 precipitation anomalies around the climatic mean over the Amazonia (10°N-20°S, 45°W-80°W),  
 512 Southwest Africa (10°S-30°S, 15°E-30°E), and Maritime Continent (20°S-20°N, 90°E-160°E).  
 513 (Bottom) Scatter plots of the WD between the observed and modeled joint PDFs of  $|\hat{\kappa}_{1,MJO}(t)|$   
 514 and  $\omega_{1,MJO}(t)$  (see Figure 4) and the pattern correlation coefficients of the Hovmöller diagram  
 515 (see Figures S7-S9) between models and observations for the (b) Amazonia, (c) Southwest  
 516 Africa, and (d) Maritime Continent. Numbers inside markers represent CMIP6 models (1-20),  
 517 reanalysis (21), and observations (22) as in Figure 3. It is seen that models that better reproduce  
 518 MJO magnitude and propagation dynamics (low WD value) also tend to better reproduce the  
 519 MJO-related precipitation variability over Amazonia and Maritime Continent, but not necessarily  
 520 in Southwestern Africa.

# Supporting Information for **Underestimated MJO in CMIP6 models**

Phong V.V. Le<sup>1,2</sup>, Clement Guilloteau<sup>1</sup>, Antonios Mamalakis<sup>1,3</sup>, and Efi Foufoula-Georgiou<sup>1,4</sup>

<sup>1</sup>Department of Civil and Environmental Engineering, University of California Irvine, CA, USA

<sup>2</sup>Faculty of Hydrology Meteorology and Oceanography, University of Science, Vietnam National University, Hanoi, Vietnam

<sup>3</sup>Department of Atmospheric Science, Colorado State University, Fort Collins, CO, USA

<sup>4</sup>Department of Earth Systems Science, University of California Irvine, CA, USA

## **Contents of this file**

1. Tables S1 to S2
2. Figures S1 to S11

**Table S1:** The selected 20 CMIP6 models used in our study with names, institutions and horizontal grid resolution of the atmospheric and ocean variables. The models were selected based on data availability at the time of writing the manuscript. The ID assigned to each model is used throughout this study.

ID	Model	Institution Name	Average grid resolution (longitude x latitude)	
			Atmosphere	Ocean
1	ACCESS-CM2	Commonwealth Scientific and Industrial Research Organisation (CSIRO), Australia	$1.87^\circ \times 1.25^\circ$	$1.0^\circ \times 1.0^\circ$
2	ACCESS-ESM1-5		$1.87^\circ \times 1.25^\circ$	$1.0^\circ \times 1.0^\circ$
3	BCC-CSM2-MR	Beijing Climate Center, Beijing, China	$1.1^\circ \times 1.1^\circ$	$1.0^\circ \times 0.78^\circ$
4	BCC-ESM1		$2.8^\circ \times 2.8^\circ$	$1.0^\circ \times 0.78^\circ$
5	CanESM5	Canadian Centre for Climate Modelling and Analysis, Environment and Climate Change Canada, BC, Canada	$2.8^\circ \times 2.8^\circ$	$1.0^\circ \times 0.62^\circ$
6	CESM2	National Center for Atmospheric Research, Boulder, CO, USA	$0.9^\circ \times 1.25^\circ$	$0.9^\circ \times 1.25^\circ$
7	CESM2-FV2		$1.9^\circ \times 2.5^\circ$	$1.9^\circ \times 2.5^\circ$
8	CESM2-WACCM		$0.9^\circ \times 1.25^\circ$	$0.9^\circ \times 1.25^\circ$
9	CESM2-WACCM-FV2		$1.9^\circ \times 2.5^\circ$	$1.9^\circ \times 2.5^\circ$
10	EC-Earth3	Consortium of various institutions from Spain, Italy, Denmark, Finland, Germany, Ireland, Portugal, Netherlands, Norway, the United Kingdom, Belgium, and Sweden	$0.7^\circ \times 0.7^\circ$	$1.0^\circ \times 0.62^\circ$
11	EC-Earth3-Veg		$0.7^\circ \times 0.7^\circ$	$1.0^\circ \times 0.62^\circ$
12	GFDL-CM4	Geophysical Fluid Dynamics Laboratory, NOAA, Princeton, NJ, USA	$1.0^\circ \times 1.0^\circ$	$0.25^\circ \times 0.16^\circ$
13	IPSL-CM6A-LR	Institut Pierre Simon Laplace, Paris, France	$2.5^\circ \times 1.25^\circ$	$1.0^\circ \times 0.54^\circ$
14	MIROC6	Japan Agency for Marine-Earth Science and Technology, Atmosphere and Ocean Research Institute, National Institute for Environmental Studies, and RIKEN Center for Computational Science, Japan	$1.4^\circ \times 1.4^\circ$	$1.0^\circ \times 0.70^\circ$
15	MPI-ESM-1-2-HAM	Max Planck Institute für Meteorologie, Forschungszentrum Jülich, University of Oxford, Finnish Meteorological Institute, Leibniz Institute for Tropospheric Research, ETH Zurich	$1.87^\circ \times 1.87^\circ$	$1.52^\circ \times 0.82^\circ$
16	MPI-ESM1-2-HR		$0.94^\circ \times 0.94^\circ$	$0.45^\circ \times 0.45^\circ$
17	MPI-ESM1-2-LR		$1.87^\circ \times 1.87^\circ$	$1.4^\circ \times 0.82^\circ$
18	MRI-ESM2-0	Meteorological Research Institute, Tsukuba, Japan	$1.1^\circ \times 1.1^\circ$	$1.0^\circ \times 0.5^\circ$
19	NESM3	Nanjing University of Information Science and Technology, Nanjing, China	$1.87^\circ \times 1.87^\circ$	$1.0^\circ \times 0.62^\circ$
20	SAM0-UNICON	Seoul National University, Seoul, Republic of Korea	$1.25^\circ \times 0.94^\circ$	$1.1^\circ \times 0.47^\circ$

**Table S2:** List of observed daily global precipitation products used for comparison.

<b>ID</b>	<b>Name</b>	<b>Abbreviation</b>	<b>Period of record</b>	<b>Spatial resolution</b>
1	Precipitation Estimation from Remotely Sensed Information using Artificial Neural Networks - Climate Data Record	PERSIANN-CDR	1983-present	$0.25^{\circ} \times 0.25^{\circ}$
2	Integrated Multi-satellitE Retrievals for GPM	IMERG	2001-present	$0.1^{\circ} \times 0.1^{\circ}$
3	Tropical Rainfall Measuring Mission (34B2)	TRMM	1998-present	$0.25^{\circ} \times 0.25^{\circ}$
4	Global Precipitation Climatology Project	GPCP	1996- present	$1.0^{\circ} \times 1.0^{\circ}$
5	CPC MORPHing technique	CMORPH	2002- present	$0.25^{\circ} \times 0.25^{\circ}$

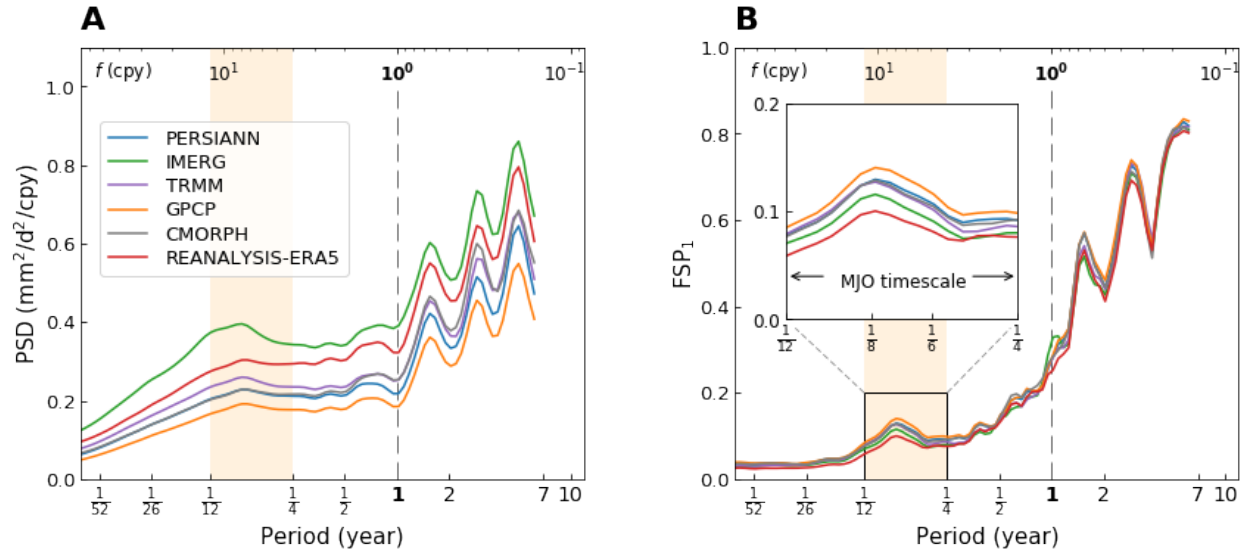


**Figure S1.** (a) Power spectral density and (b) Fraction of spectral power explained by the first wavelet principal component (wPC1) of daily precipitation rate obtained from 5 different observed datasets and the reanalysis products during the common period 2002-2019. The highest and lowest values of power spectral density is found in the IMERG and GPCP, respectively, but all observed datasets are in good agreement in terms of capturing the MJO mode. The MJO timescale (yellow shaded vertical bands) ranges from 1-3 months. Frequency  $f$  in cycles per year (cpy) is shown in the top horizontal axes.

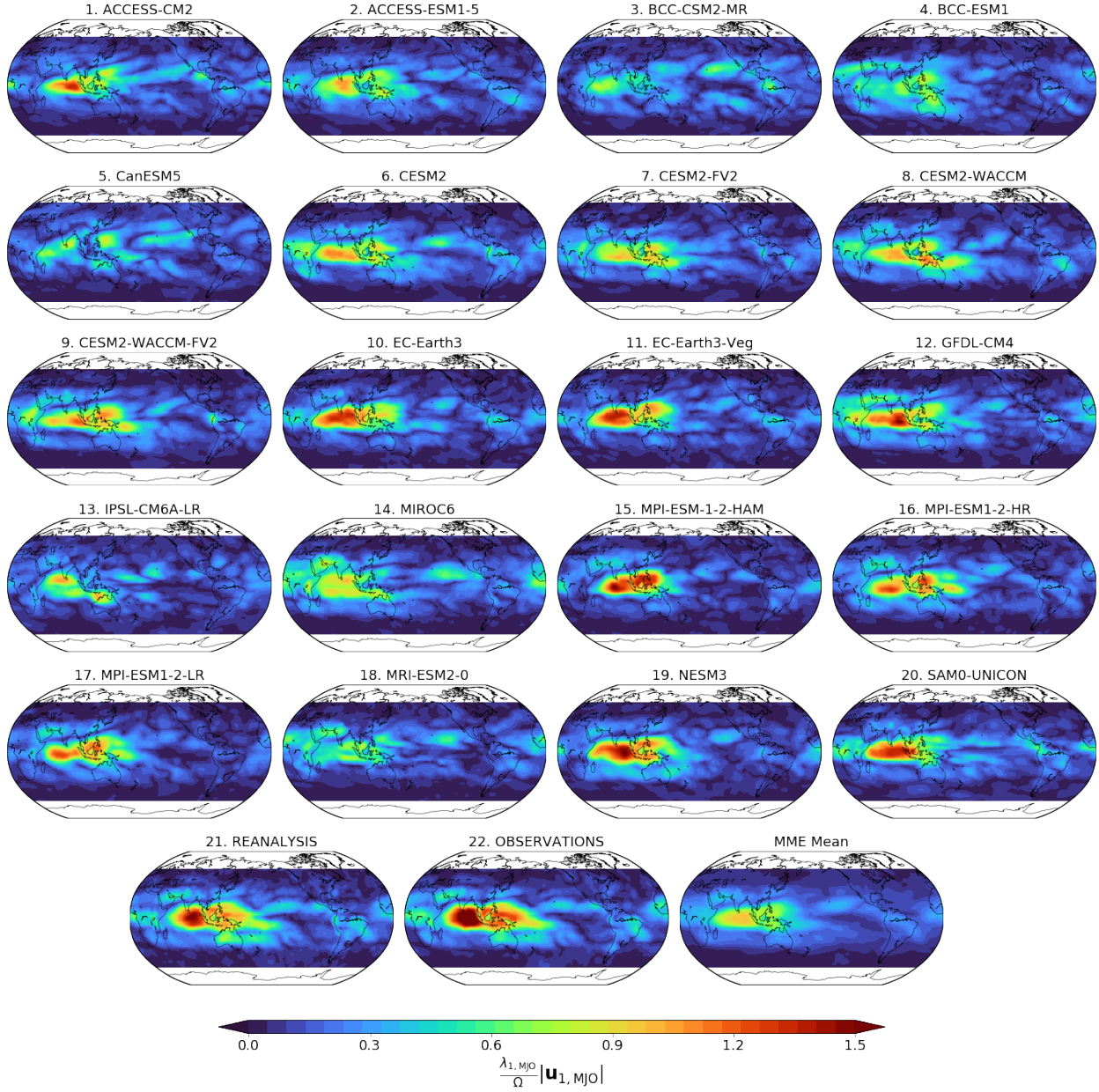


**Figure S2.** Spatial patterns of the modulus (magnitude) of the MJO band-integrated first complex eigenvector  $\mathbf{u}_{1,MJO}$  of OLR for the 20 CMIP6 models, reanalysis, and observations. MME Mean represents the mean of the 20 models. The map is shown for the unit-norm eigenvector with a scaling factor  $\frac{\lambda_{1,MJO}}{\Omega}$  representing the contribution of wPC1 to the total energy in the MJO frequency band, with  $\Omega = \sqrt{\frac{tr(\Lambda_{MJO})}{N}}$ . See text for definitions.

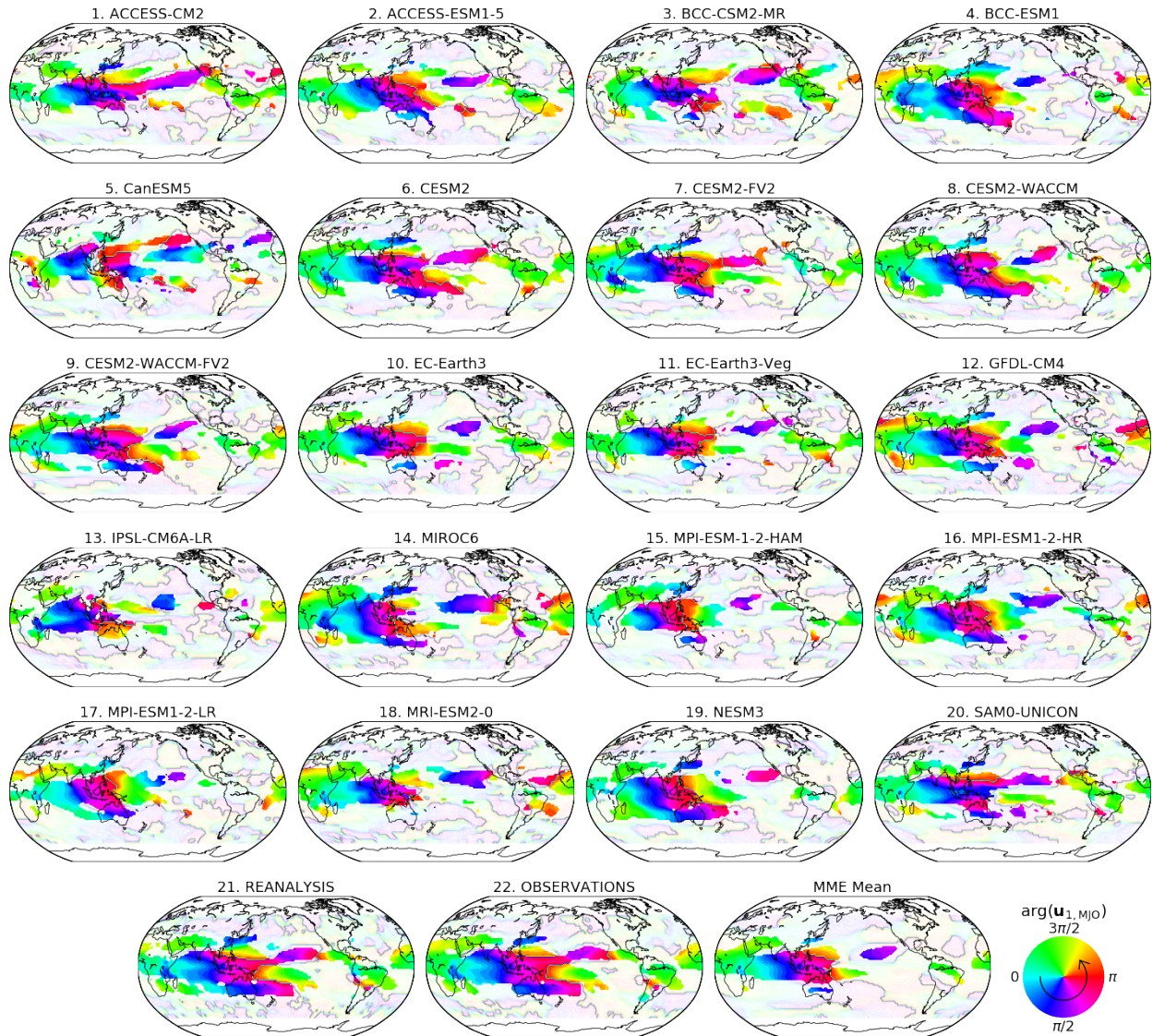


**Figure S3.** Spatial patterns of the argument (phase) of the MJO band-integrated first complex eigenvector  $\mathbf{u}_{1,MJO}$  of OLR for 20 CMIP6 models, reanalysis, and observations. MME Mean represents the mean of 20 models. The counter-clockwise, circular arrow in the colorscale indicates the direction of propagation of the extracted waves.

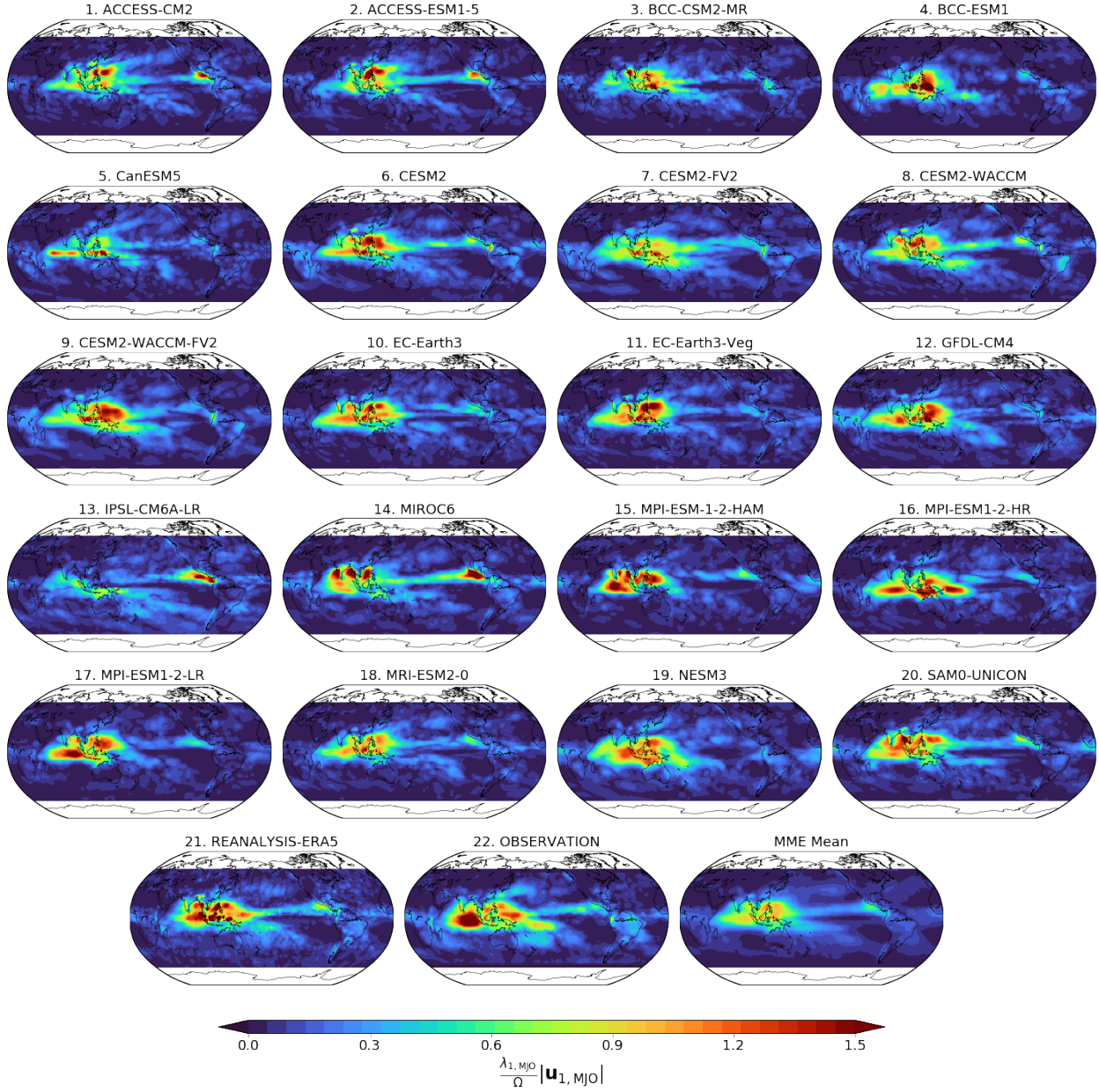


**Figure S4.** Spatial patterns of the modulus (magnitude) of the MJO band-integrated first complex eigenvector  $\mathbf{u}_{1,MJO}$  of PPT for the 20 CMIP6 models, reanalysis, and observations. MME Mean represents the mean of the 20 models. The map is shown for the unit-norm eigenvector with a scaling factor  $\frac{\lambda_{1,MJO}}{\Omega}$  representing the contribution of wPC1 to the total energy in MJO frequency band, with  $\Omega = \sqrt{\frac{tr(\Lambda_{MJO})}{N}}$

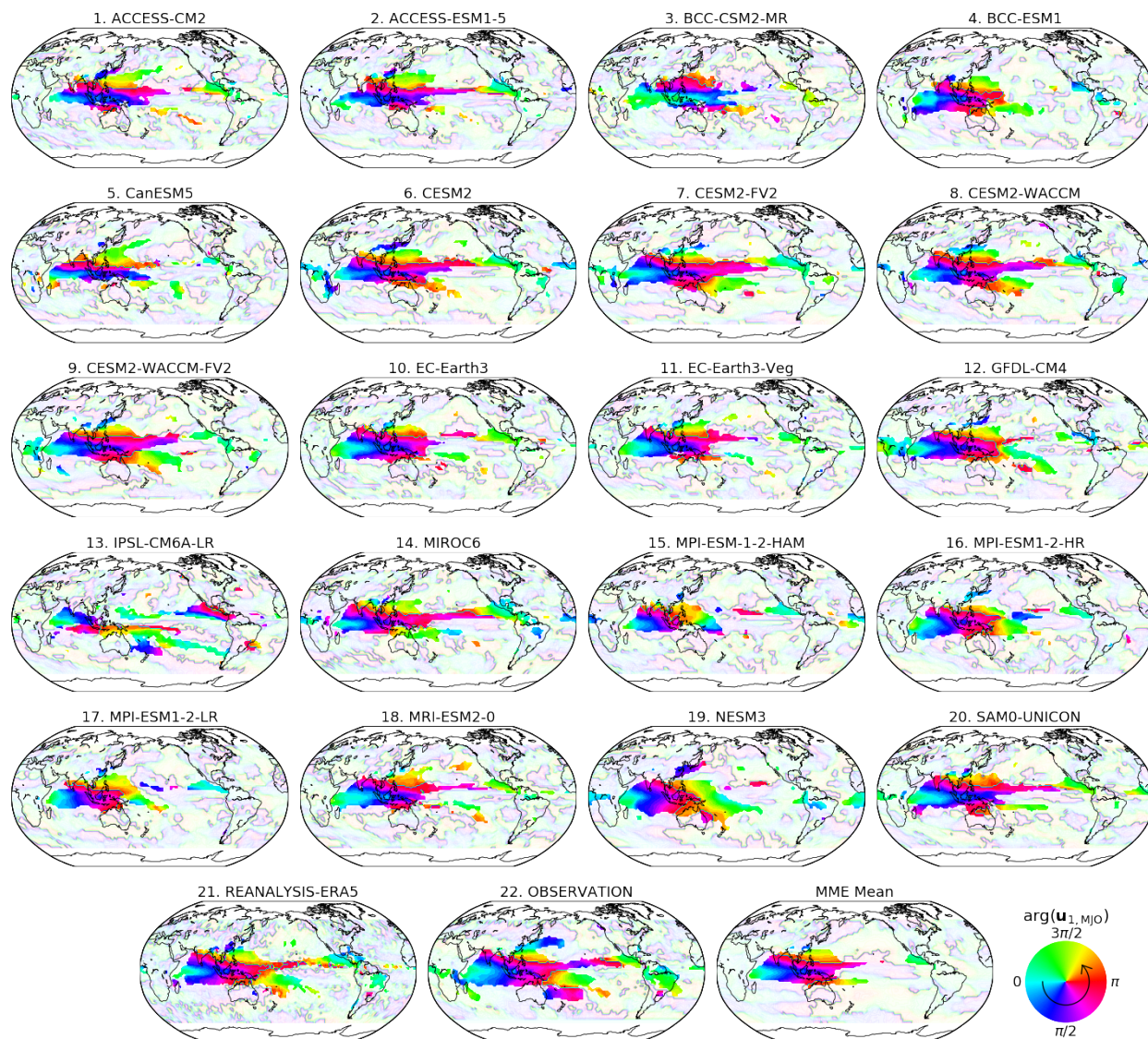


**Figure S5.** Spatial patterns of the argument (phase) of the MJO band-integrated first complex eigenvector  $\mathbf{u}_{1,MJO}$  of PPT for 20 CMIP6 models, reanalysis, and observations. MME Mean represents the mean of 20 models. The counter-clockwise, circular arrow in the colorscale indicates the direction of propagation of the extracted waves.

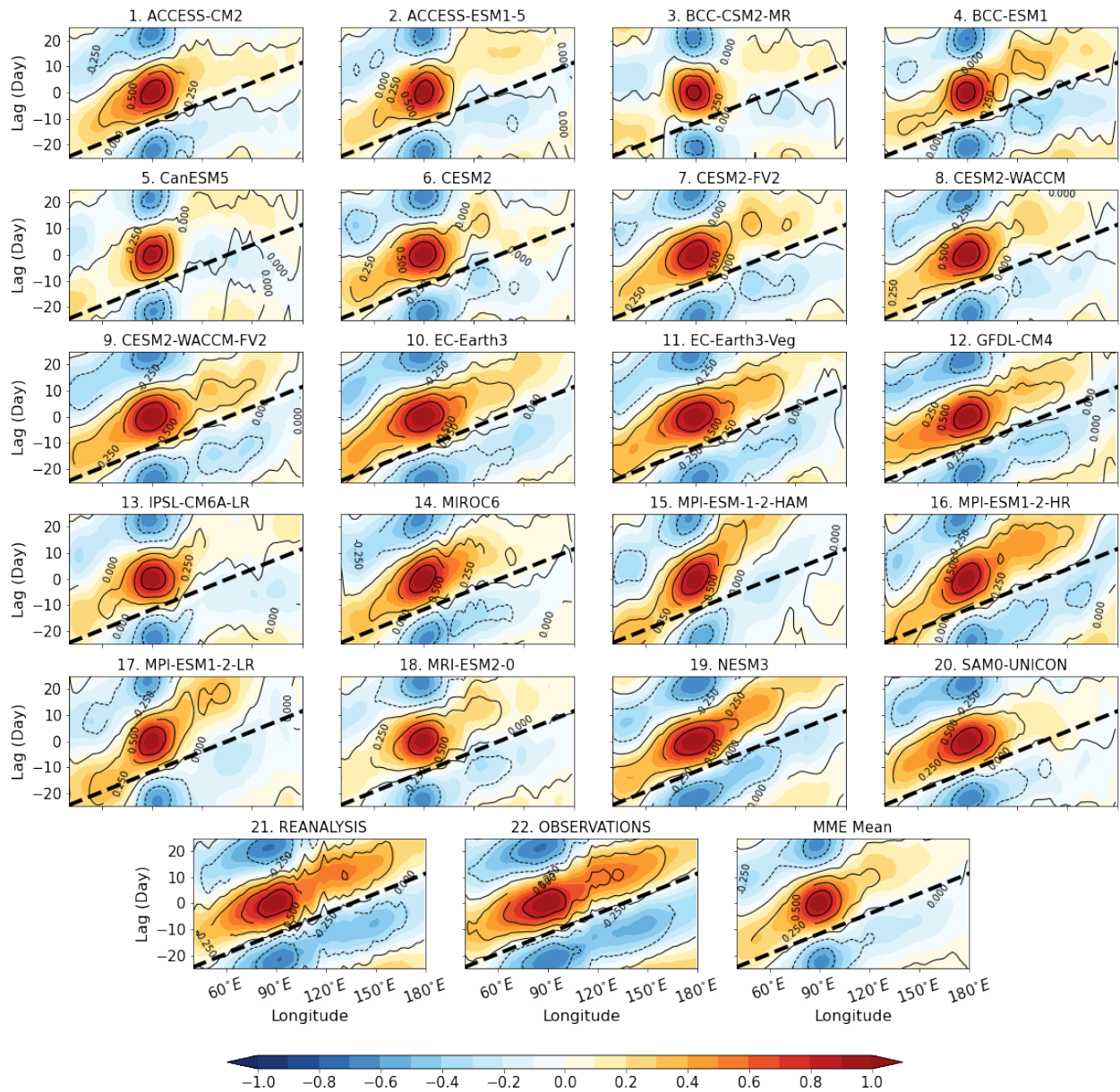


**Figure S6.** Lag-longitude diagram of  $10^{\circ}\text{S}$ - $10^{\circ}\text{N}$ -averaged OLR anomalies (colors) and PPT anomalies (contours) reconstructed within the MJO frequency band (30-90 days) against the corresponding OLR and PPT anomalies at the Indian Ocean reference region ( $10^{\circ}\text{S}$ - $10^{\circ}\text{N}$ ,  $80^{\circ}$ - $100^{\circ}\text{E}$ ) from 1983-2014. The reconstruction of OLR and PPT anomalies was performed through inverse wavelet transform of the wPC1 time series  $\kappa_{1,f}$  for frequencies  $f$  within the MJO frequency band. Black dashed lines indicate an eastward propagation speed of 5 m/s.

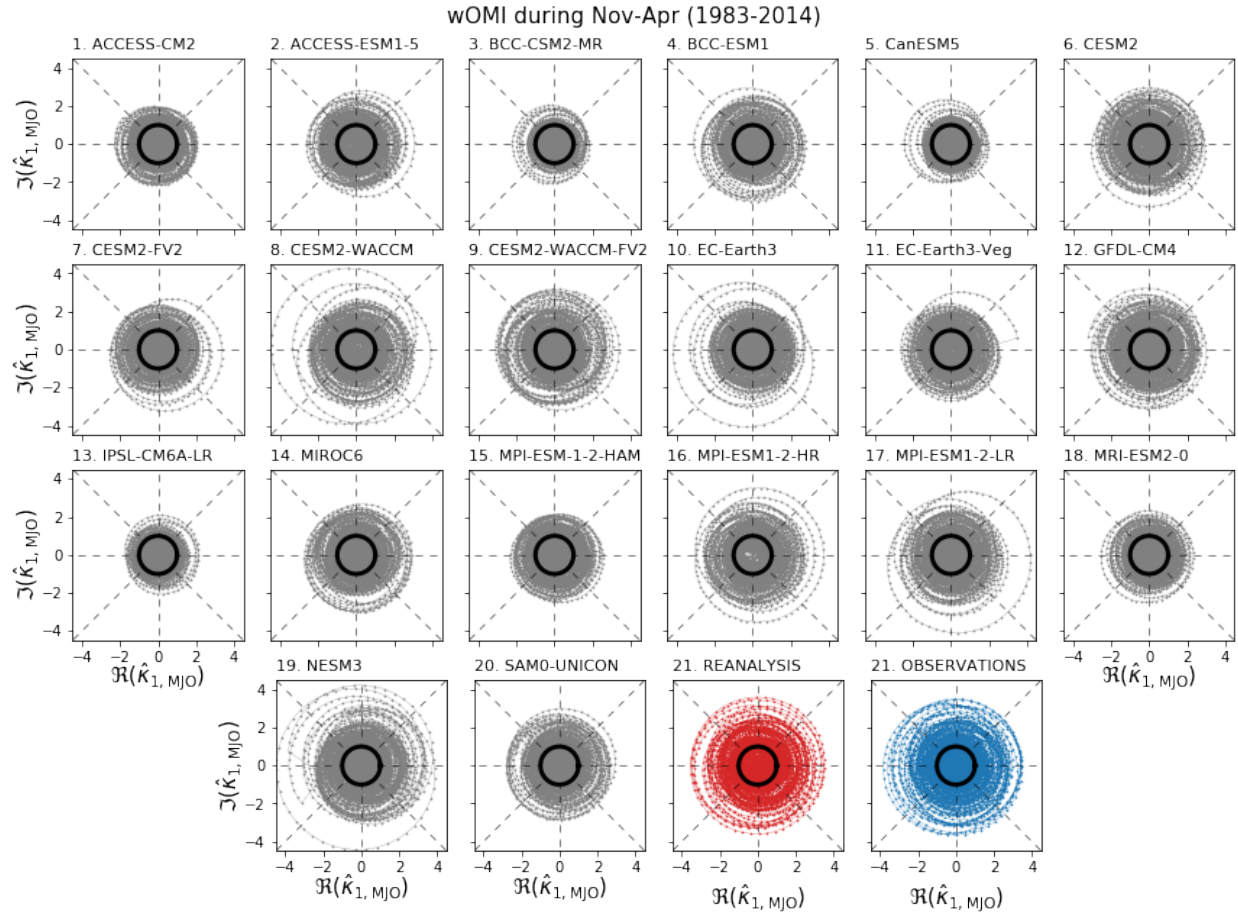


**Figure S7.** Comparison of wsPCA-based OLR MJO index (wOMI)  $\hat{\kappa}_{1, \text{MJO}}$  reproduced by 20 CMIP6 models, reanalysis products, and observations. The wOMI plots are shown during boreal winter season (Nov-Apr) from 1983-2014. It can be seen that a large number of models underestimate the amplitude of MJO.

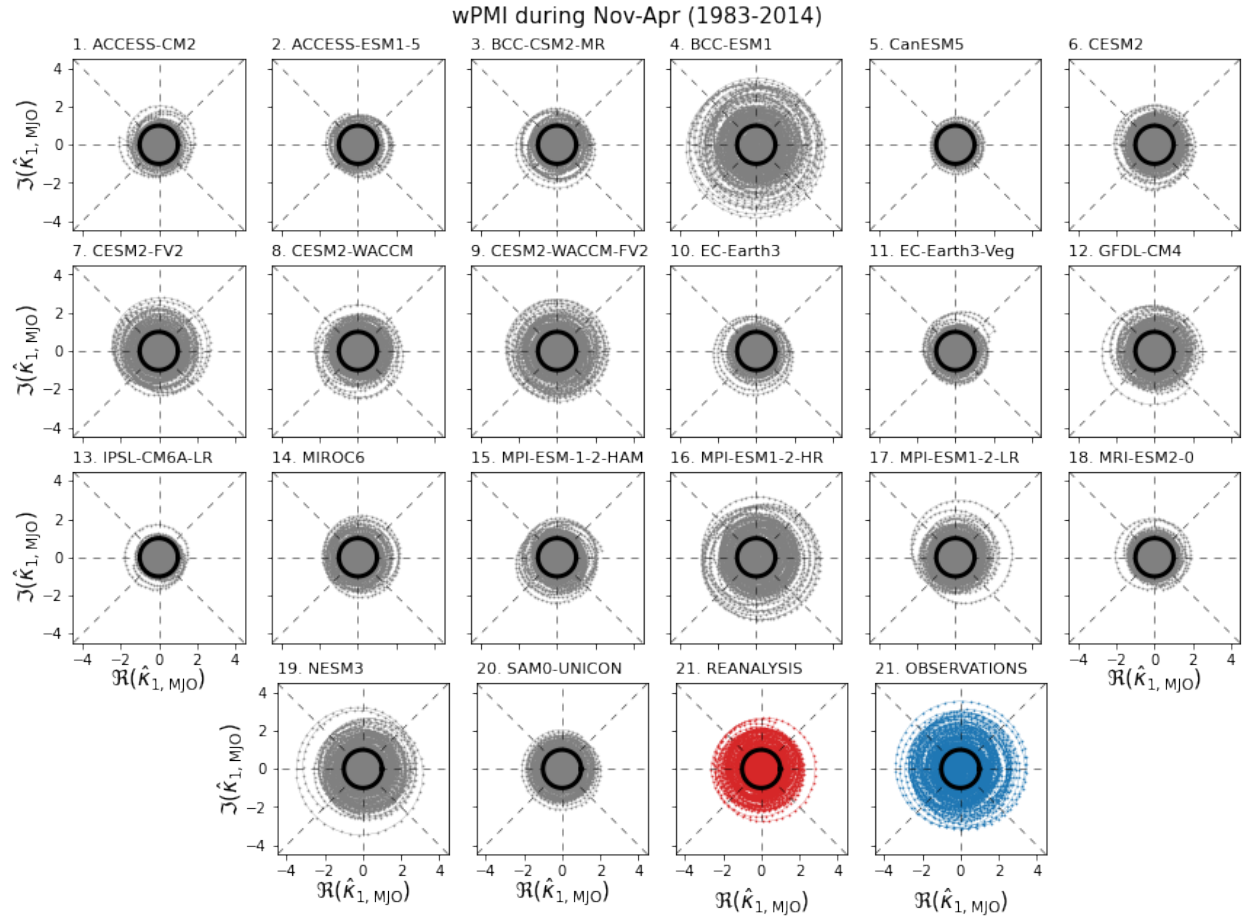


**Figure S8.** Comparison of wsPCA-based PPT MJO index (wPMI)  $\hat{\kappa}_{1, \text{MJO}}$  reproduced by 20 CMIP6 models, reanalysis products, and observations. The wPMI plots are shown during boreal winter season (Nov-Apr) from 1983-2014. Similar to wOMI, it can be seen that a large number of models underestimate the amplitude of MJO using the wPMI.

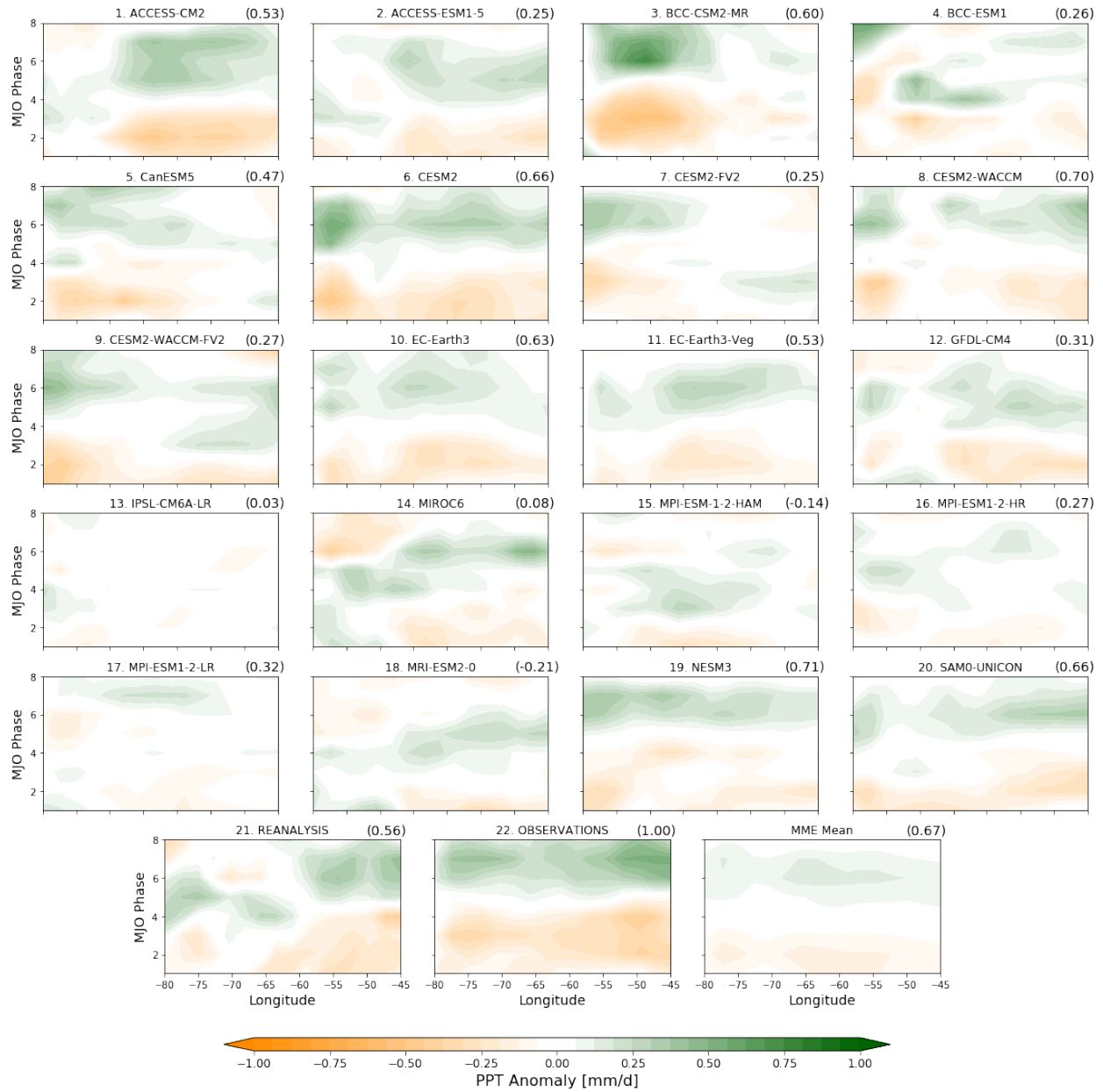


**Figure S9.** Hovmöller phase-longitude diagrams of PPT anomalies in the Amazonia (10°N-20°S, 45°W-80°W) for 20 CMIP6 models, reanalysis, and observations. MME Mean represents the mean of models. Numbers in parentheses represent the correlation coefficients of the phase-longitude patterns with the pattern obtained from the observations.

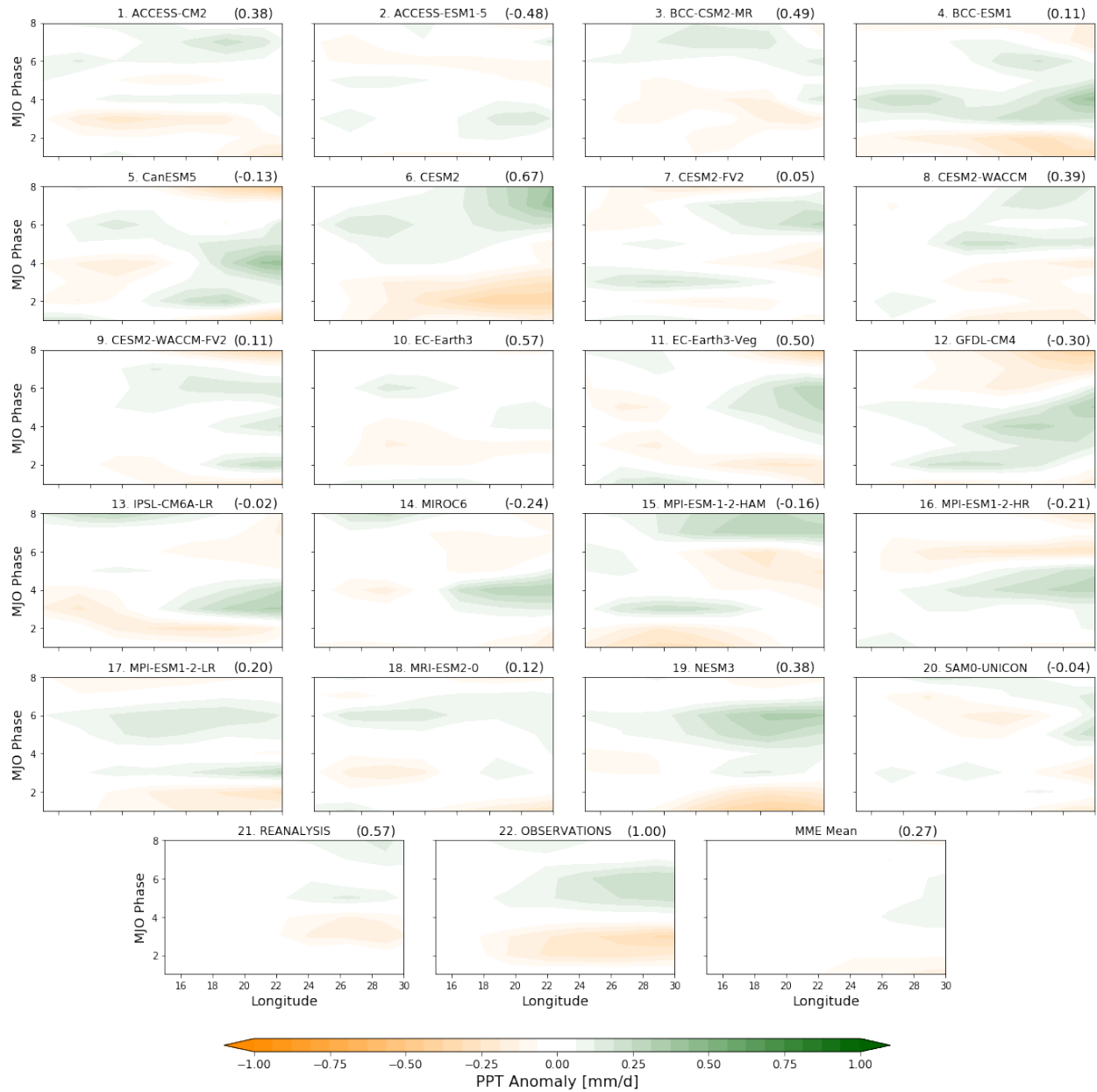


**Figure S10.** Hovmöller phase-longitude diagram of PPT anomalies in the Southwest Africa (10°S-30°S, 15°E-30°E) for 20 CMIP6 models, reanalysis, and observations. MME Mean represents the mean of models. Numbers in parentheses represent the correlation coefficients of the phase-longitude patterns with the pattern obtained from the observations.

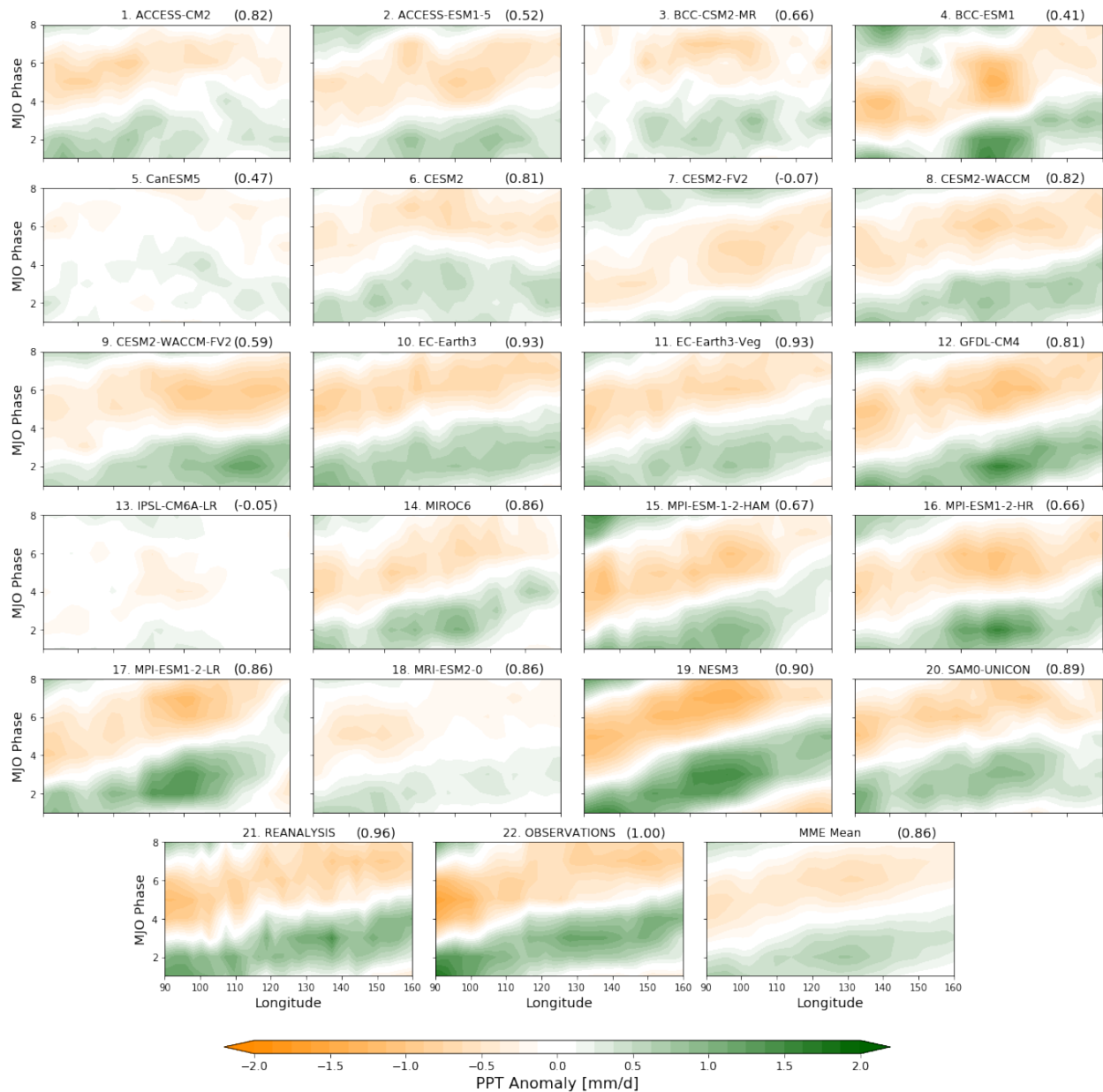


**Figure S11.** Hovmöller phase-longitude diagram of PPT anomalies in the Maritime Continent (20°S-20°N, 90°E-160°E) for 20 CMIP6 models, reanalysis, and observations. MME Mean represents the mean of models. Numbers in parentheses represent the correlation coefficients of the phase-longitude patterns with the pattern obtained from the observations.